ACS APPLIED MATERIALS & INTERFACES

www.acsami.org

Research Article

Sb_2S_3 Thin-Film Solar Cells Fabricated from an Antimony Ethyl Xanthate Based Precursor in Air

Jako S. Eensalu,* Sreekanth Mandati, Christopher H. Don, Harry Finch, Vinod R. Dhanak, Jonathan D. Major, Raitis Grzibovskis, Aile Tamm, Peeter Ritslaid, Raavo Josepson, Tanel Käämbre, Aivars Vembris, Nicolae Spalatu, Malle Krunks,* and Ilona Oja Acik

Cite This: *ACS Appl. Mater. Interfaces* 2023, 15, 42622−42636

Read Online

ACCESS | Metrics & More | Article Recommendations | Supporting Information

ABSTRACT: The rapidly expanding demand for photovoltaics (PVs) requires stable, quick, and easy to manufacture solar cells based on socioeconomically and ecologically viable earth-abundant resources. Sb_2S_3 has been a potential candidate for solar PVs and the efficiency of planar Sb_2S_3 thin-film solar cells has witnessed a reasonable rise from 5.77% in 2014 to 8% in 2022. Herein, the aim is to bring new insight into Sb_2S_3 solar cell research by investigating how the bulk and surface properties of the Sb_2S_3 absorber and the current−voltage and deep-level defect characteristics of solar cells based on these films are affected by the ultrasonic spray pyrolysis deposition temperature and the molar ratio of thiourea to SbEX in solution. The properties of the Sb_2S_3 absorber are characterized by bulk- and surface-sensitive methods. Solar cells are characterized by temperature-dependent current−voltage, external quantum efficiency, and deep-level transient spectroscopy measurements. In this paper, the first thin-film solar cells based on a planar Sb_2S_3 absorber grown from antimony ethyl xanthate (SbEX) by ultrasonic spray pyrolysis in air are demonstrated. Devices based on the Sb_2S_3 absorber grown at 200 °C, especially from a solution of thiourea and SbEX in a molar ratio of 4.5, perform the best by virtue of suppressed surface oxidation of Sb_2S_3, favorable band alignment, Sb-vacancy concentration, a continuous film morphology, and a suitable film thickness of 75 nm, achieving up to 4.1% power conversion efficiency, which is the best efficiency to date for planar Sb_2S_3 solar cells grown from xanthate-based precursors. Our findings highlight the importance of developing synthesis conditions to achieve the best solar cell device performance for an Sb_2S_3 absorber layer pertaining to the chosen deposition method, experimental setup, and precursors.

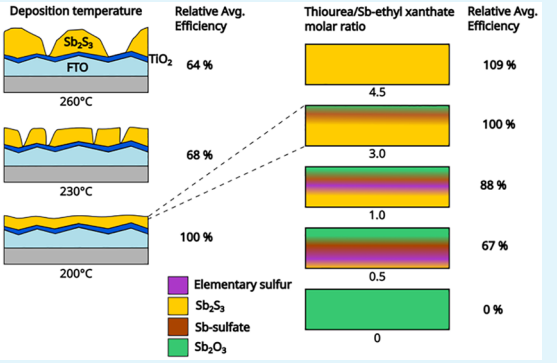

KEYWORDS: *Antimony sulfide, chemical synthesis, photovoltaics, solar cells, spray pyrolysis, thin films*

INTRODUCTION

The Sun imparts 10 000 times more energy to the Earth than humankind consumes.[1] Photovoltaics (PVs) provide direct clean renewable energy for restoring the ecosystem while sustaining humane living conditions. Increasing clean PV capacity requires stable, quick, and easy to manufacture solar cells from socioeconomically and ecologically viable earth-abundant resources. Emerging PVs are best suited for tandem cells with silicon and standalone semitransparent PV modules. As the absorber layer is the most critical component in PVs, a fitting inorganic absorber material should be sought. Antimony sulfide, a stable inorganic semiconductor[2] composed of abundant and environmentally benign S ($0.09 kg^{-1}) and Sb ($11.4 kg^{-1}), is an emerging PV absorber.[3] The covalent anisotropic 1D-ribbon structure[2,4,5] of Sb_2S_3 gives rise to its melting point of 550 °C,[2] allowing crystallization of the absorber below 300 °C.[5,6] Furthermore, Sb_2S_3 is an excellent thin-film solar absorber due to its direct band gap of 1.7 eV,[2,5] a refractive index in excess of 2.2,[5,6] and an absorption coefficient of 10^4−10^5 cm^{-1} in visible light.[4]

In addition, the single-phase composition,[2,7] facile synthesis by chemical methods,[4] long-term stability, and corrosion resistance[2,7] are the main qualities that Sb_2S_3 offers to the development of environmentally sustainable and affordable PVs. The efficiency of planar Sb_2S_3 thin film solar cells has risen from 5.77% in 2014 to 8% in 2022.[8,9] Enhancing their efficiency requires overcoming a large V_{OC} deficit,[4] by amelioration of the intrinsic point defects inducing self-trapping in the absorber,[10] proper engineering of vertical grain growth, increasing the lateral grain size,[11,12] and interface engineering. Moreover, dewetting[6,13] and tuning of the precursor chemistry[6,9,11−16] must be addressed. In broad terms, the cutting-edge development of

Received: June 13, 2023
Accepted: August 3, 2023
Published: August 28, 2023

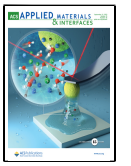

Sb_2S_3 solar cells has split into three main directions: maximizing solar cell efficiency for standalone applications,[9] maximizing the ratio of solar cell efficiency to absorber thickness targeting sustainable exploitation of antimony,[6] a critical raw material,[17−19] and development of semitransparent devices for use in building-integrated PVs or as the top cell in two-cell tandem PVs.[20,21] Further understanding in these directions depends on first-principles calculations and defect engineering studies.

Synthesis conditions largely determine the efficiency of Sb_2S_3 solar cells.[4] Antimony alkyldithiocarbamates have yielded highly efficient solar cells based on a chemically grown continuous and large-grained Sb_2S_3 absorber layer,[11,12] up to an efficiency of 7.1%.[22,23] solar cells in mesoporous TiO_2 configuration based on Sb_2S_3 synthesized from antimony xanthate i.e. alkyldithiocarbonate have reached only 3.7% efficiency after sulfurizing the Sb_2S_3 absorber with thiourea.[24] Furthermore, xanthate-based planar Sb_2S_3 devices have not been reported. Considering the lower decomposition temperature of the xanthate-based precursor, it should be explored on a level with the carbamates. Previously, our group has reported that Sb_2S_3 films can be grown from antimony ethyl xanthate (SbEX) by ultrasonic spray pyrolysis only with additives such as thiourea or thioacetamide that shield the surface from oxidation during deposition.[25] Therefore, we endeavor to deduce how the PV absorber properties of planar Sb_2S_3 films grown from antimony xanthates differ from those grown from carbamates. Moreover, understanding the thermal and chemical history of the constituent layers of solar cells is vital to boosting the efficiency further by surmounting the many challenges ahead.

Hence, the aim is to bring new insight into Sb_2S_3 solar cell research by investigating how the bulk and surface properties of the Sb_2S_3 absorber, the current−voltage, and deep-level defect characteristics of solar cells based on these films are affected by the ultrasonic spray pyrolysis deposition temperature and the molar ratio of thiourea to SbEX in solution. Devices based on the Sb_2S_3 absorber grown at 200 °C, especially from a solution of thiourea and SbEX in a molar ratio of 4.5, perform the best by virtue of suppressed surface oxidation of Sb_2S_3, favorable band alignment and Sb-vacancy concentration, continuous film morphology, and a suitable film thickness of 75 nm, achieving up to 4.1% power conversion efficiency, which is the best efficiency to date for planar Sb_2S_3 solar cells grown from xanthate-based precursors.

EXPERIMENTAL SECTION

The chemicals used in this study are listed in Table S1 in the Supporting Information.

Sample Preparation. Fluorine-doped tin oxide (FTO) covered 2.1 mm glass slides (MSE Supplies, TEC7) were cleaned by consecutively ultrasonicating in a bath of detergent water, 50/50 methanol−acetone, and isopropyl alcohol for 10 min, followed by immersion in boiling deionized water for 10 min. A compact TiO_2 film was deposited by ultrasonic spray pyrolysis at 350 °C from a solution of 0.1 M titanium tetraisopropoxide and 0.4 M acetylacetone dissolved in ethanol, followed by heat treatment in air at 450 °C for 30 min to obtain anatase, as reported previously.[15,25,26] The average thicknesses of the active layers in the glass/FTO/TiO_2 stack are 577 nm for FTO (density, ρ 7.0 g cm^{-3}) and 77 nm for TiO_2 (ρ 4.17 g cm^{-3}) as calculated from XRF data.[27] The Sb_2S_3 absorber was grown using ultrasonic spray pyrolysis (USP) at a nebulization frequency of 1.7 MHz and a power of 200 W. The compressed air flow velocity was 3.7 cm s^{-1}, and the solution flow rate was 11 μL cm^{-2} min^{-1} through a circular vertical nozzle (ϕ 100 mm) positioned 13 mm above the substrate surface, moving in a cyclical pattern over a 170 mm × 170 mm area (effective area 268 cm^2). For the deposition temperature series, Sb_2S_3 absorbers were grown at temperatures of 200, 230, and 260 °C for 20 min from a solution of 90 mM thiourea (TU) and 30 mM SbEX dissolved in acetonitrile. Finally, the TU concentration series was deposited at a temperature of 200 °C for 20 min from a solution of TU/SbEX in molar ratios of 0.5, 1.0, 1.5, 3.0, 4.5, and 6.0 dissolved in acetonitrile at a constant 30 mM SbEX concentration. After the deposition of Sb_2S_3, the samples were heat-treated in a tube furnace at 270 °C for 10 min in nitrogen flowing at 1.1 cm s^{-1}, at an average heating and cooling rate of 8 °C min^{-1}. Solar cells were prepared by depositing a solution of 1 wt % regioregular poly(3-hexylthiophene-2,5-diyl) (P3HT) dissolved in chlorobenzene onto the FTO/TiO_2/Sb_2S_3 stack by spin coating at 350 rpm for 4 s, accelerating at 2000 rpm s^{-1} to 3000 rpm for 20 s. P3HT was activated by heat treatment in a tube furnace at 170 °C for 5 min in nitrogen flowing at 2.1 cm s^{-1}, at an average heating and cooling rate of 12 °C min^{-1}. The stack was completed by thermally evaporating a gold back contact through a metal mask with ϕ 4 mm circles, thereby defining the active cell area as 12.6 mm^2.

Characterization. The structure and phase composition were characterized by XRD (Rigaku Ultima IV, θ−2θ, Cu Kα_1 λ = 1.5406 Å, 40 kV, 40 mA, step 0.02°, 5° min^{-1}, Si strip detector D/teX Ultra) and Raman spectroscopy (Horiba Labram HR 800, ∼143 μW μm^{-2}, 532 nm YAG:Nd laser). In accordance with best practices,[28] in this study we used the space group No. 62 *Pbnm* setting (ICDD #42-1393) for the Miller indexing of planes in Sb_2S_3 for which a = 11.09 ± 0.03 Å, b = 11.326 ± 0.017 Å, and c = 3.826 ± 0.015 Å and the covalently bonded ribbons lie parallel to the c vector, [001]. Optical spectra were measured using a UV−vis−NIR spectrophotometer (Jasco V-670, integrating sphere, air reference). Local elemental composition and morphology were measured with a combined energy dispersive X-ray spectrometer (Bruker spectrometer, ESPRIT 1.8, 7 kV) and scanning electron microscopy (Zeiss HR FESEM Ultra 55, 4 kV) system. Integral elemental composition was measured from a circle of ϕ 10 mm with a wavelength-dispersive X-ray fluorescence (XRF) spectrometer (Rigaku ZSX-400). Elemental composition was measured from the Sb L_α-line, S K_α-line, Cl K_α-line, and K K_α-line. The pure FTO substrate was analyzed as a homogeneous mixture of O (48.1 wt %), Si (33.2 wt %), Na (8.23 wt %), Ca (6.28 wt %), Mg (2.46 wt %), K (0.919 wt %), Al (0.73 wt %), S (0.0804 wt %), and Cl (0.0203 wt %).

X-ray photoelectron spectroscopy (XPS) spectra of a heat-treated Sb_2S_3 film, grown at 200 °C using TU/SbEX 3.0, were measured with a PSP Vacuum Technology hemispherical electron-energy analyzer equipped with monochromated Al Kα radiation ($h\nu$ = 1486.6 eV). Spectrometer calibration was performed by measuring both the $3d_{5/2}$ and Fermi edge of a clean polycrystalline silver foil Ar^+ sputtered under vacuum.[29] The spectrometer was operated with an overall resolution of ±0.1 eV. High-resolution XPS spectra were fitted with a Voigt (GL(X)) at a Gaussian:Lorentzian ratio tuned for an optimal fit. XPS spectra of heat-treated Sb_2S_3 films, grown at 200 °C with a variable TU/SbEX ratio, were measured with a SPECS PHOIBOS 150 2D-DLD hemispherical electron-energy analyzer equipped with a Mg Kα ($h\nu$ = 1253.6 eV) source.[30] High-resolution XPS spectra collected with a pass energy of 50 eV and a step of 0.1 eV were fitted using CasaXPS (v2.3) software. Charging-induced offset in XPS spectra collected with SPECS PHOIBOS was corrected by calibrating with adventitious carbon (C 1s C−C, 284.5 eV). The Sb 3d, Sb 4d, and S 2p spin orbit split doublet peaks were separated based on literature by 9.40, 1.25, and 1.20 eV, respectively.[31] A Shirley background subtraction was applied in all XPS spectra. The width of the same species of doublets was constrained to be the same. XPS peaks were fitted with the Voigt-like symmetric Lorentzian (LA) line shape (1.53, 243).

Room-temperature current−voltage (I−V) curves of solar cells were measured with a factory-calibrated solar simulator (Wavelabs LS2, LED light source), a metal mask with an adjustable aperture area, and a source meter under AM1.5G, 100 mW cm^{-2} conditions. Temperature-dependent I−V curves were measured with a closed-cycle He cryostat (Janis CCS-150) using a halogen lamp. The position of the halogen lamp was calibrated to match the short-circuit current obtained with the solar simulator under AM1.5G conditions at room temperature as a starting point. The external quantum efficiency (EQE) spectra were

https://doi.org/10.1021/acsami.3c08547
ACS Appl. Mater. Interfaces 2023, 15, 42622−42636

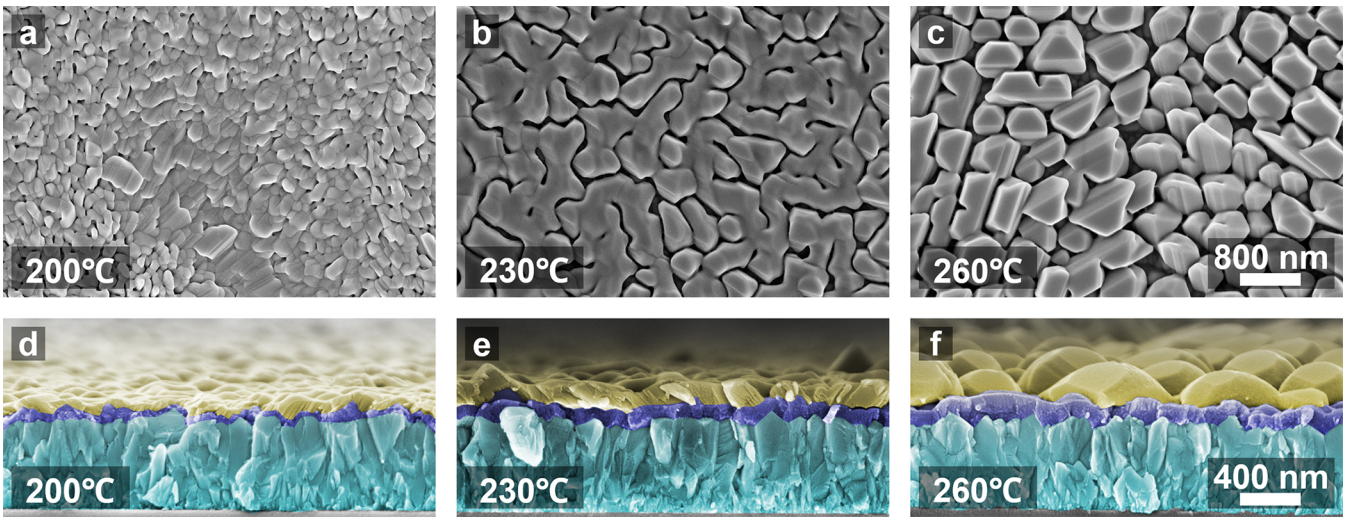

Figure 1. Top-down and cross-sectional SEM images of heat-treated Sb_2S_3 absorbers (in yellow) grown onto an FTO (in cyan)/TiO_2 (in dark blue) substrate at deposition temperatures of (a, d) 200 °C, (b, e) 230 °C, and (c, f) 260 °C.

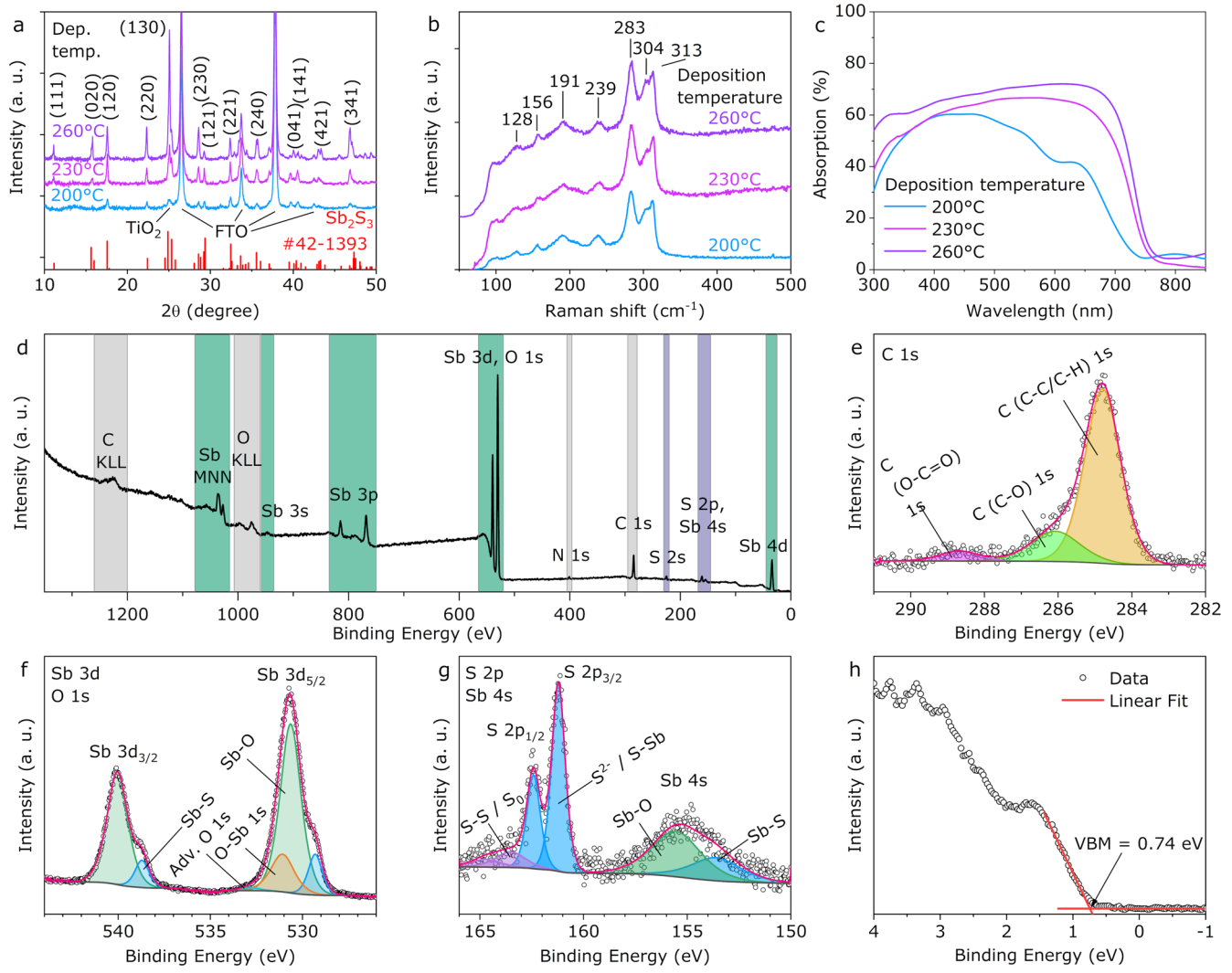

Figure 2. (a) XRD patterns, (b) Raman spectra, and (c) absorption spectra of heat-treated Sb_2S_3 absorbers grown at 200, 230, and 260 °C, TU/SbEX 3.0. (d) X-ray photoelectron spectroscopy (XPS) survey spectrum, XPS results of (e) C 1s region, (f) Sb 3d and O 1s regions, and (g) S 2p and Sb 4s regions, and (h) valence band (VB) onset of the heat-treated Sb_2S_3 absorber grown at 200 °C.

https://doi.org/10.1021/acsami.3c08547
ACS Appl. Mater. Interfaces 2023, 15, 42622−42636

measured without a white light bias using a monochromated light source at 0 V voltage bias (Newport 300 W xenon lamp, 69911 with a Cornerstone 260 monochromator), a digital lock-in detector (Merlin), and a factory-calibrated Si reference detector. The short-circuit current density (J_{SC}) was integrated from EQE spectra under AM1.5G conditions.

Deep level transient spectroscopy (DLTS) analysis was conducted using a Phystech FT1230 HERA DLTS system connected to a Linkam HFSX350 liquid nitrogen fed cryostat with a measurement range of 85−275 K. The device back contact field was used to probe the deep level content by applying reverse and pulse biases of 4 and 1 V, respectively. A pulse duration of 10 μs was applied with resultant transients compared over three period widths of 4.8, 48, and 480 ms with values for the trap energies and capture cross section extracted from an Arrhenius assessment using the three period widths and a series of correlator functions.[32]

The ionization energy level value of the studied materials was determined by using a self-built photoelectron emission spectroscopy (PES) system. The system consists of a white light source (ENERGETIQ Laser Driven Light Source (LDLS EQ-99)), a monochromator (Spectral Products DK240 1/4 m), and an electrometer (Keithley 617). The measurements were carried out in a vacuum ($\sim 2 \times 10^{-5}$ mbar) at room temperature. The distance between the sample and the electrode that collected emitted electrons was about 2 cm, and a voltage of 50 V was applied between the sample and the electrode. The measurements were carried out in the spectral range between 3.5 and 6.5 eV with a 0.05 eV step. The ionization energy was determined as the threshold energy in the photoelectron emission yield spectral dependence.

RESULTS AND DISCUSSION

Effect of Sb_2S_3 Deposition Temperature. Heeding our thermal analysis study,[33] a solution of TU/SbEX 3.0 is deposited onto glass/FTO/TiO_2 substrates, at 200 °C, the point after the first decomposition step, 230 °C, the point before the second decomposition step, and 260 °C, the point after the second decomposition step of SbEX.

The surface of the heat-treated Sb_2S_3 absorber grown at 200 °C is continuous (Figure 1a,d), composed of 100−300 nm wide and 40−90 nm thick slanted grains. The Sb_2S_3 absorber grown at 230 °C is 70−190 nm thick, with 150−300 nm wide grains showing signs of dewetting (Figure 1b,e), crystallizing at the expense of the surrounding material. The surface of the absorber grown at 260 °C consists of partially merged 200−1000 nm wide and 350 nm thick domes (Figure 1c,f). Notably, the catenoids and menisci connecting dewetted grains (Figure S1a,b) hint at liquid-phase interactions and capillary action during deposition and crystallization. Dewetting intensifies at a deposition temperature beyond 200 °C possibly because the transient liquid thiourea phase, which prevents oxidation and facilitates coalescence of amorphous Sb_2S_3 at 200 °C, decomposes faster.[15,25] Dewetting has also been observed in Sb_2S_3 layers grown by spray pyrolysis at 250 °C from a solution of TU/$SbCl_3$.[34]

According to XRD (Figure 2a), the signal can be attributed only to crystalline orthorhombic Sb_2S_3, and the glass/FTO/TiO_2 substrate is detected in the heat-treated samples. Experimentally, an increase in Scherrer (120) crystallite size from 43 ± 6 to 55 ± 3 and 60 ± 3 nm for the 200, 230, and 260 °C samples is observed, respectively, indicating that the absorber grown at a higher deposition temperature crystallizes further. Raman spectra of the heat-treated films (Figure 2b) yield vibrational bands centered at 128, 156, 191, 239, 283, 304, and 313 cm^{-1}, matching crystalline Sb_2S_3.[5]

Increasing the deposition temperature of Sb_2S_3 from 200 to 230 and 260 °C causes a red shift in visible light absorption and a general increase in absorption (Figure 2c). Transmittance, however, increases at the same time in the 350−500 nm range (Figure S2a). The 200 °C Sb_2S_3 film reflects 40% of visible light and shows thin-film interference (Figure S2b), whereas the films grown at 230 and 260 °C reflect 30% without interference. The band gaps of the 200, 230, and 260 °C Sb_2S_3 absorbers are 1.77, 1.67, and 1.66 eV from $(\alpha h\nu)^2$ vs photon energy curves (Figure S2c) or 1.80, 1.72, and 1.71 eV via sigmoidal fits of absorption, respectively. We ascribe the decrease in band gap to the increase in Sb_2S_3 crystallite size representing more complete crystallization due to less carbonaceous precursor decomposition residue remaining in the film, based on the thermal analysis of SbEX.[33]

The XPS survey spectrum shows peaks of Sb, S, O, C, and N at the surface of the Sb_2S_3 film grown at 200 °C (Figure 2d). High-resolution XPS spectra are collected in the regions of C 1s (Figure 2e), S 2p and Sb 4s (Figure 2f), and Sb 3d and O 1s (Figure 2g).

The C 1s region presented in Figure 2e consists primarily of peaks attributed to C−C/C−H bonding, with a lesser contribution of C−O and O−C═O bonding, ascribed to exposure to hydrocarbons and CO_2 in ambient air. The primary doublet signal present in Sb 3d spectra (Figure 2f) originates from the high binding energy (BE) of native oxide species (Sb_2O_3) (green),[16,35−37] while the low-BE shoulder (purple) is attributed to the expected lattice Sb_2S_3. The significant intensity of the oxide component observed here suggests a plausible sulfur deficiency during the film deposition process. Although from these surface-sensitive XPS results it is not clear how much of the oxidation is induced by the deposition itself, is manifested in the bulk film, or is due to atmospheric exposure of the surface postdeposition as observed in CSS-grown Sb_2Se_3 films.[38] It should be noted that the O 1s core level overlaps the Sb $3d_{5/2}$ peak position, for which two species are identified: O−Sb (Sb_2O_3) and adventitious oxygen weakly adsorbed on the surface.

Figure 2g shows the XPS spectra obtained in the S 2p core level region, which incorporates Sb 4s because of their close binding energy proximity (fitting results are given in Table S2). The most intense signal is attributed to S−Sb (Sb_2S_3) (blue) with a $2p_{3/2}$ and $2p_{1/2}$ doublet separation of 1.2 eV, which is well established.[16,39] An additional doublet species shifted to a higher BE is identified here as elemental S (purple, Figure 2f). This four-peak, two-species signal is present elsewhere in CSS-grown Sb_2S_3[14] with a S−Sb−elemental S separation of 2.3 eV, however, the interpretation from Guo et al. appears to misidentify $2p_{3/2}$ and $2p_{1/2}$ components, with no mention of the origins of these two species. In the case of Sb_2Se_3 it has been claimed based on XPS data that elemental Se remains on the surface after Sb_2Se_3 oxidation to Sb_2O_3.[35,37]

Finally, the valence band onset is measured as 0.74 eV below the Fermi level via linear extrapolation to the low-binding-energy minima (Figure 2h). Assuming the 1.75 eV (see Figure S2a,b) extracted optical band gap to be (i) the same as the electrical band gap and (ii) correct, this indicates that E_F is below the middle of the band gap, implying that the material possesses p-type conductivity. While we acknowledge surface band bending must be considered which will affect the valence band maximum (VBM) E_F, a recent study on p-type Sb_2Se_3 demonstrated that due to downward band bending at the surface, the bulk actually showed an enhanced p-type conductivity.[40] In addition, Figure 2h shows a secondary onset at ~2 eV that we propose is caused by the heavy film oxidation

https://doi.org/10.1021/acsami.3c08547
ACS Appl. Mater. Interfaces 2023, 15, 42622−42636

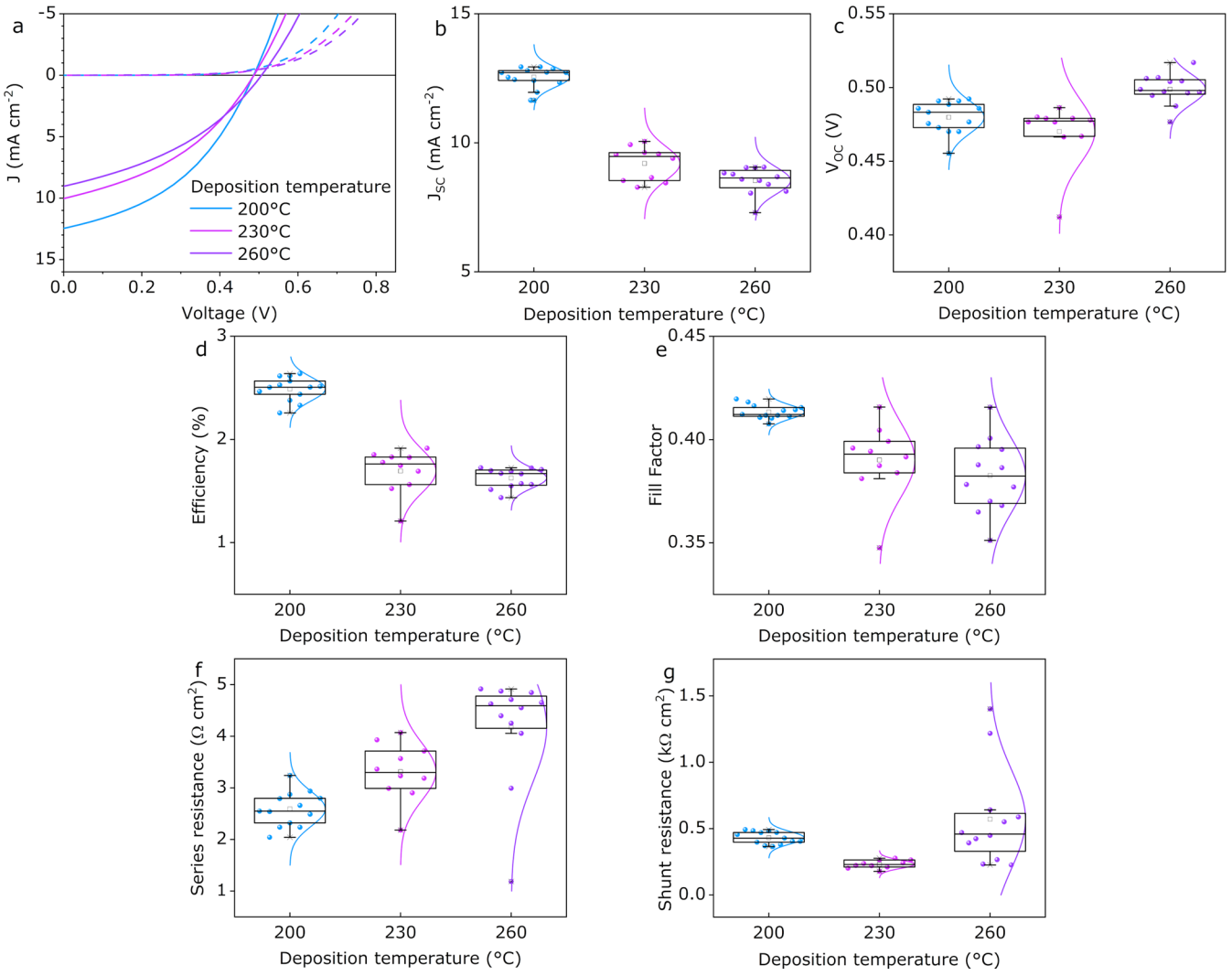

Figure 3. (a) $J-V$ curves of the best devices. Statistics on (b) J_{SC}, (c) V_{OC}, (d) efficiency, (e) fill factor, (f) R_S, and (g) R_{SH} of solar cells measured in the dark or under AM1.5G conditions as a function of Sb_2S_3 deposition temperature.

Table 1. Solar Cell Output Characteristics as a Function of the Sb_2S_3 Deposition Temperature

Sb_2S_3 deposition temperature, °C	V_{OC}, mV	J_{SC}, mA cm^{-2}	FF, %	η, %	R_S, Ω cm^2	R_{SH}, kΩ cm^2
200	492	12.9	42	2.6	2.0	0.49
	479 ± 11[a]	12.5 ± 0.4	41 ± 1	2.5 ± 0.1	2.6 ± 0.3	0.43 ± 0.05
230	486	10.1	39	1.9	3.7	0.22
	470 ± 21	9.2 ± 0.7	39 ± 2	1.7 ± 0.2	3.3 ± 0.6	0.23 ± 0.03
260	506	9.0	38	1.7	4.1	1.2
	499 ± 10	8.5 ± 0.5	38 ± 2	1.6 ± 0.1	4.2 ± 1.1	0.57 ± 0.37

[a]Average and standard deviation.

demonstrated in the core-level spectra. This is further evidenced by the presence of oxide-induced tail states which soften the VB onset, shown to disappear upon cleaving of an oxidized Sb_2Se_3 crystal surface.[37]

According to XRF data, the S/Sb atomic ratios are 1.25, 1.33, and 1.29 for the heat-treated Sb_2S_3 absorbers grown at 200, 230, and 260 °C, respectively, indicating a sulfur-deficient bulk composition likely resulting from partial oxidation (Figure 2f,g) that possibly elevates the concentration of e.g. Sb_S and V_S point defects.[41] The average film thicknesses are 56, 129, and 205 nm (ρ = 4.6 g cm^{-3}) for the heat-treated Sb_2S_3 absorbers grown at 200, 230, and 260 °C, respectively, as calculated from the Sb L_α XRF signal. The linear increase in film thickness by 2.5 nm per 1 °C of rise in deposition temperature signals that the yield of Sb_2S_3 increases with temperature, possibly due to a higher decomposition yield of SbEX into insoluble Sb_2S_3.

Dark and illuminated current−voltage ($I-V$) scans of the best devices based on Sb_2S_3 absorbers grown at 200, 230, and 260 °C are presented for reference (Figure 3a); statistics are shown in Figure 3b−g, and numeric data are shown in Table 1. As the

https://doi.org/10.1021/acsami.3c08547
ACS Appl. Mater. Interfaces 2023, 15, 42622−42636

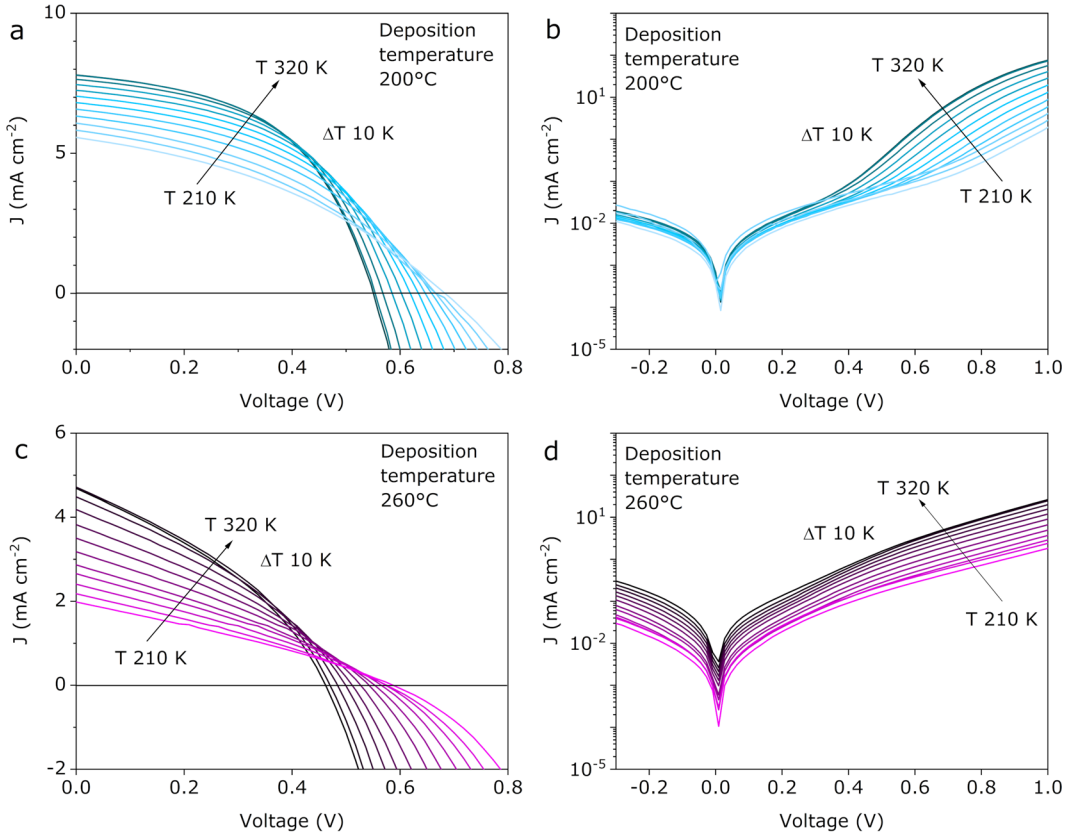

Figure 4. Temperature dependent (a, c) illuminated and (b, d) dark $I-V$ curves of solar cells based on Sb_2S_3 grown at (a, b) 200 and (c, d) 260 °C.

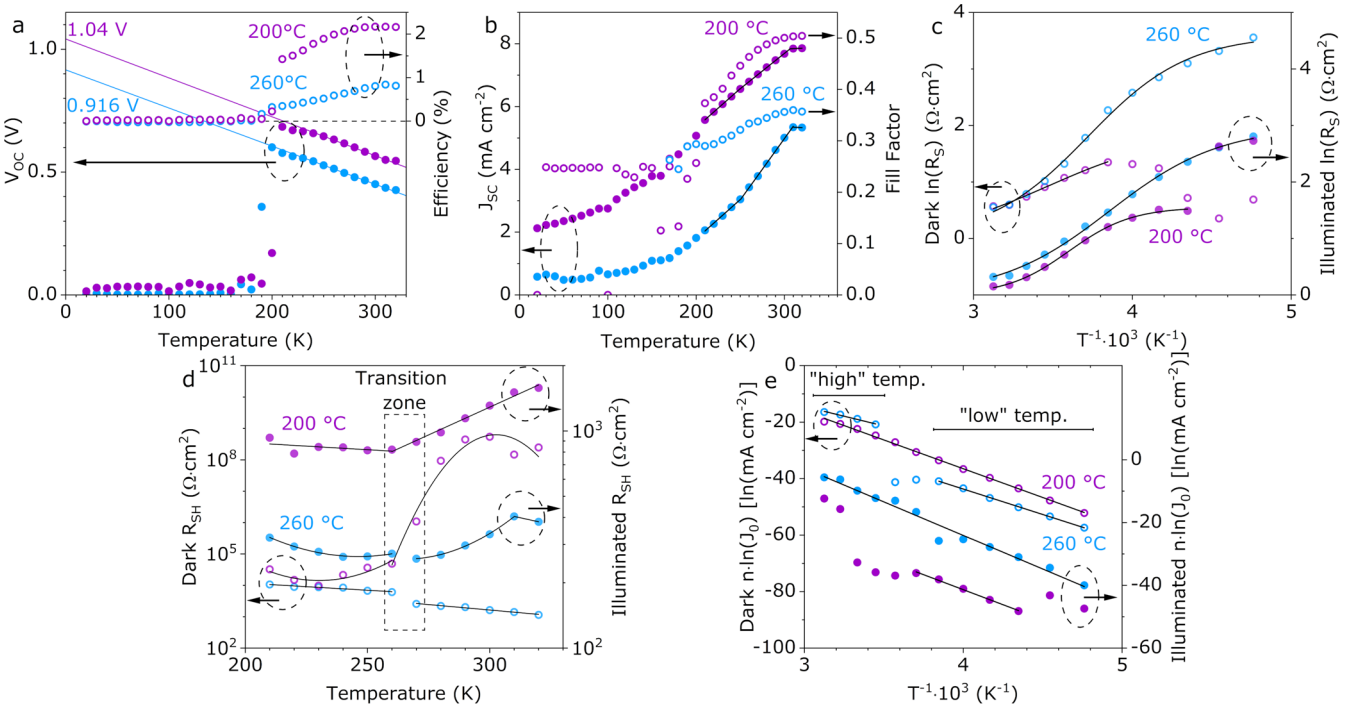

Figure 5. Temperature dependence of (a) V_{OC}, J_{SC}, (b) fill factor and efficiency, (c) series resistance, (d) shunt resistance, and (e) ideality factor corrected saturation current of solar cells based on Sb_2S_3 grown at (a, b) 200 and (d, e) 260 °C. Numerical data are given in Tables S3−S6.

deposition temperature is increased from 200 to 230 and 260 °C, the average J_{SC} decreases from 12.5 to 9.2 and 8.5 mA cm^{-2}, respectively (Figure 3b). V_{OC} is 470−500 mV regardless of the deposition temperature (Figure 3c). Efficiency follows J_{SC}, decreasing from 2.5 to 1.7 and 1.6% as the deposition temperature is increased from 200 to 230 and 260 °C, respectively (Figure 3d). As the deposition temperature is increased by 60 °C (Figure 3e), the slight drop in fill factor from

https://doi.org/10.1021/acsami.3c08547
ACS Appl. Mater. Interfaces 2023, 15, 42622−42636

41 to 38% is attributed to an increase in R_S (Figure 3f), because R_{SH} is constant (Figure 3g). As the deposition temperature is increased, R_S increases from 2.6 to 3.3 and 4.2 Ω cm^2. The increase in R_S and the decrease in current density, as the deposition temperature is increased, are attributed to the redistribution of the absorber material into clusters of up to 4 times thicker more resistive separate grains (Figure 1a−f) and the formation of a parallel junction between TiO_2 and P3HT that does not generate photocurrent. The $(EQE{\cdot}h\nu)^2$-derived band gap (Figure S2d) correlates with the optical band gap (Figure S2c).

The coevolution of the average light absorption, J_{SC}, XRF-derived film thickness, and R_S (Figure S3) was analyzed by Pearson cross-correlation. As the absorber thicknesses for the 230 and 260 °C devices (see Figure 1e,f) exceed the charge carrier diffusion length of 200 nm reported for Sb_2S_3,[42] the loss in photocurrent is likely related to increased bulk recombination.

Spraying a thicker Sb_2S_3 film to increase J_{SC} is not quite straightforward, as J_{SC} (Figure S4a) and efficiency (Figure S4b) saturate after 20 min of deposition time, whereas V_{OC} (Figure S4c) slightly increases while the fill factor (Figure S4d) decreases. The film deposited for 10 min transmits blue light after heat treatment (Figure S5a), and the TiO_2 signal appears in the Raman spectrum at 145 cm^{-1} (Figure S5b). Therefore, the film is thin and discontinuous. Transmittance decreases and its edge red shifts in the films grown for longer times, indicating an increase in optical thickness despite a consistent band gap (Figure S5c). The J_{SC} saturation is attributed to the high surface activity of the freshly sprayed TiO_2 substrate that repeatably facilitates crystallization of Sb_2S_3 as up to 50 μm wide, thick pyramidal silvery grains (Figure S6a−d) during deposition that deliver less J_{SC} than the thinner flat-plate-shaped grains obtained via heat treatment (Figure S6e−h). TiO_2 surface modification will likely allow increasing the absorber thickness by suppressing the pyramidal crystallization, as we have observed in some preliminary tests.

The recombination behavior of the solar cells is investigated via $I-V-T$ measurements under halogen lamp illumination (Figure 4a,b) and in the dark (Figure 4c,d). The deposition temperature of the absorber layer affects the second diode, seen at >0.4 V forward bias. The dominant recombination modes, calculated by extrapolating V_{OC} to 0 K,[43] are 1.04 and 0.916 V (Figure 5a) for the 200 and 260 °C devices, respectively. Therefore, interface recombination dominates in these solar cells, apparently increasing when the absorber is grown at a higher temperature, meaning that the absorber interfaces deteriorate. Curiously, temperature-dependent V_{OC} of fully inorganic Sb_2S_3 solar cells has only ever been reported down to 210 and 140 K, with a built-in voltage of 1.08 or 0.97 V.[44,45] However, whenever tunneling is present the ideality factor becomes temperature dependent, turning V_{OC} vs T nonlinear.[46] Therefore, the activation energy calculated by extrapolating V_{OC} might be inaccurate and should be supplemented with Φ_B calculated from n and J_0. Such an approach is especially useful if the $I-V$ temperature dependence is available over a limited range. As the temperature is decreased from 320 K, efficiency peaks at 2.2% and 0.77% at 310 K for the 200 and 260 °C Sb_2S_3 devices, respectively (Figure 5a), whereas below 210 K device $I-V$ behavior changes from diode to resistor. Below 310 K, efficiency, J_{SC}, and fill factor decrease linearly in the range of 270−210 K for both cells (Figure 5a,b). The transition to resistor at 210 K marks short-circuiting or a sudden decrease in capacitance, possibly caused by delamination owing to incompatible lattice parameters at interfaces or undesirable phase transitions in one or more of the component layers.

The series resistance of both devices under illumination and in the dark (see Figure 5c) is fitted with a simple exponential dependence[46]

$$R_S(T) = R_{S0}/(1 + \beta \exp(-E_a/kT)) \quad (1)$$

where R_S is the series resistance, R_{S0} a temperature-independent series resistance, β a prefactor, E_a the activation energy, k Boltzmann's constant, and T temperature.

The activation energy is 230 ± 46 meV in the dark and 437 ± 26 meV under illumination for the 200 °C Sb_2S_3 cell, which could be caused by the carriers becoming trapped at the interface, leading to a band offset. This activation energy is often attributed to the back contact barrier height. Notably, after initially increasing, R_S in the dark decreases at temperatures below 260 K, hinting at a behavior more complex than can be explained by this model. The activation energy is a more consistent 274 ± 16 meV in the dark and 248 ± 10 meV under illumination for the 260 °C Sb_2S_3 cell, implying a rather light-insensitive behavior.

In the dark (Figure 5d), R_{SH} of the 200 °C Sb_2S_3 device decreases from 10^8 Ω cm^2 at 300 K to 10^4 Ω cm^2 at 260 K. R_{SH} under illumination decreases linearly from 320 to 260 K and then increases. R_{SH} of the 260 °C Sb_2S_3 device increases in the dark at a constant linear slope as the temperature is decreased and follows a bowl-shaped curve under illumination. As R_{SH} jumps in the transition zone of 270−260 K in both devices in the dark and under illumination, a thermally activated phase transition process must occur. This sudden change is *a priori* attributed to the phase transition of P3HT known to occur near 263 K.[47] The observed anomaly is possibly related to the nonlinear temperature dependence of the dielectric permittivity of Sb_2S_3 near 270 K.[48] The overall behavior of the shunt resistance is dominated by the synthesis history of the absorber layer notwithstanding.

Further information can be extracted from the temperature dependence of the saturation current density J_0[49]

$$n \ln J_0 = n \ln J_{00} - \frac{\Phi_B}{kT} \quad (2)$$

where J_{00} is a weakly temperature dependent prefactor and Φ_B the activation energy of the saturation current. The slope of the plot of $n \ln J_0$ vs $1/kT$ is expected to correspond to that of Φ_B (Figure 5e). The calculated activation energy values are 1.75 ± 0.02 eV in the dark and 1.65 ± 0.06 eV under illumination for the 200 °C device, close to the Sb_2S_3 band gap of 1.75 eV. The 0.1 eV smaller activation energy under illumination reveals that interface recombination is the dominant mechanism, which is ascribed to Fermi level pinning or narrowing of the band gap at the interface.[46] For the 260 °C Sb_2S_3 device, the activation energy is 1.18 ± 0.11 eV at the "high" temperature, 1.55 ± 0.02 eV at the "low" temperature in the dark, and 1.84 ± 0.09 eV under illumination (Figure 5e). As $\Phi_B > E_g$, bulk recombination within the absorber is likely in balance with or dominates interface recombination. Notably, Φ_B calculated from the temperature dependence of n and J_0 is larger than when V_{OC} is extrapolated for both devices. These Sb_2S_3 solar cells operate efficiently at −53 to +47 °C, corresponding to the temperate, arid, and continental climate zones,[50] which account for some of the most densely populated areas on Earth, whereas perform-

https://doi.org/10.1021/acsami.3c08547
ACS Appl. Mater. Interfaces 2023, 15, 42622−42636

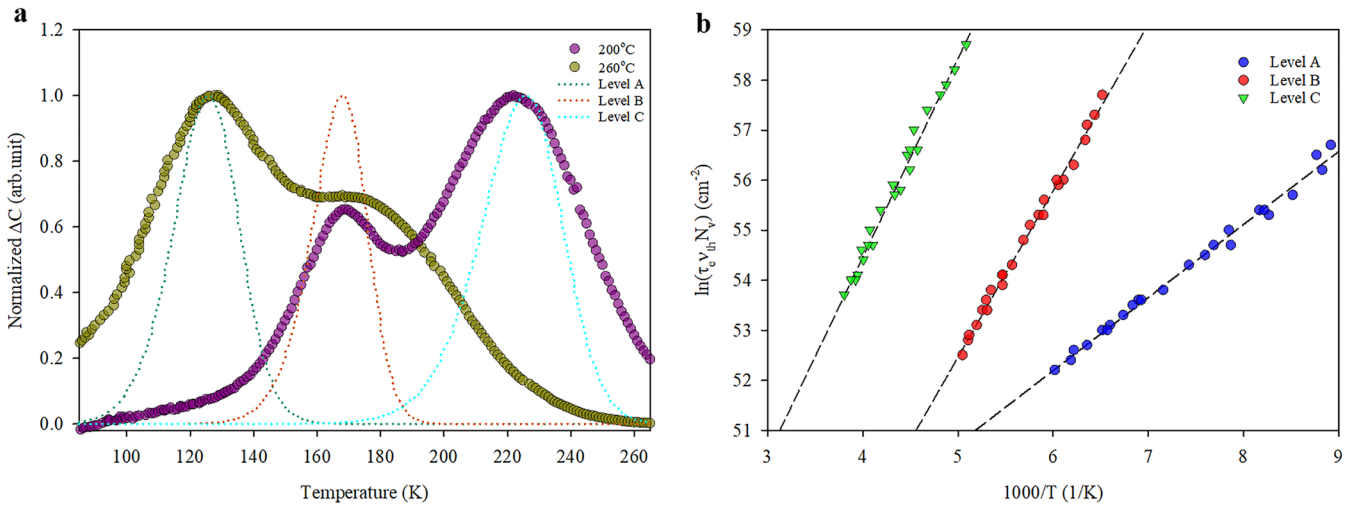

Figure 6. Deep level transient spectroscopy (DLTS) analysis for Sb_2S_3 solar cells with absorber layers deposited at 200 and 260 °C showing (a) normalized ΔC values extracted from capacitance transients as a function of temperature and (b) Arrhenius determination of trap energy and capture cross section with values given in Table 2. Determined values were then used to model spectra overlaid on measurement data in Figure 6a.

ance is apparently limited by interface and tunneling recombination.

Deep level transient spectroscopy (DLTS) analysis is conducted on the two devices with deposition temperatures of 200 and 260 °C, the least similar under $J-V$ analysis. After initial DLTS testing, it is found that sweeping the main junction field, the typical approach for PV device measurement,[32,51] produces capacitance transients with a poor signal-to-noise ratio, making extraction of defect properties impossible. An alternative approach is to take advantage of the device's back contact field to produce a bias sweep. This is found to produce significantly higher quality capacitance transients, with Figure 6a showing extracted ΔC values as a function of temperature for a 48 ms period width measurement. Capacitance values are normalized to allow a simple and direct comparison of the two sample spectra. Defect levels are observed as peaks in the ΔC spectra, where the emission rate of the defect state is maximized within the parameters of the particular measurement setup (i.e., changing the period width or effective rate window will shift the peak position). By tracking the peak positions observed for a range of correlator functions applied to the recorded capacitance transients, an Arrhenius assessment can be constructed (Figure 6b), with the energetic position of trap levels, E_T, and associated capture cross sections, σ_p, being extracted (Table 2). Because the absorber material is p-type, E_T values are measured with respect to the valence band maxima. Using the extracted values, the equivalent spectra modeled for those trap states are overlaid on the DLTS spectra in Figure 6a. In both samples, three distinct defect levels are observed but with a shift in prominence of the levels between the two temperatures. For the 200 °C sample, a deeper level at 345 meV is dominant, while for the 260 °C sample, a shallower 123 meV level is more pronounced. A level of 284 meV is effectively invariant between the two samples. The presence of a more dominant deep level in the 200 °C sample would be anticipated to increase recombination, lower carrier lifetime, and reduce device V_{OC}. This agrees well with the $I-V$ data for these samples where, despite the overall device performance being lower, the 260 °C sample shows an improved V_{OC}, which we may infer is due to the reduced presence of the 345 meV deep defect level. While the source of these defect levels cannot be interrogated directly via DLTS, instead reference to density functional theory (DFT) calculations of defect formation energies can offer some insight. Defect formation energy calculations for Sb_2S_3 show a triplet of defect levels in an energy range similar to those observed here which are caused by the various charge states of the antimony vacancy (V_{Sb}) defect.[14] Hence, what we may infer from this is that the change in deposition temperature has likely caused a modification of the V_{Sb} content between the two absorbers, necessitating further study on the topic.

Table 2. Defect Level Energies (E_T) and Capture Cross Section (σ_p) Values Extracted from DLTS Analysis

defect level	E_T, meV	σ_p, cm^{-2}
level A	123 ± 3	$(1.10 \pm 0.28) \times 10^{-19}$
level B	284 ± 4	$(2.24 \pm 0.61) \times 10^{-16}$
level C	345 ± 8	$(1.49 \pm 0.81) \times 10^{-17}$

Effect of Thiourea Concentration. Having established that 200 °C is the optimal deposition temperature for Sb_2S_3 with regard to absorber conformity and solar cell efficiency, the concentration of thiourea is varied from 0.5 to 6.0 TU/SbEX at constant Sb^{3+} concentration in the following experiments.

SEM reveals that the heat-treated Sb_2S_3 absorber grown from the TU/SbEX 0.5 solution is discontinuous and is at most 50 nm thick (Figure 7a,g). TU/SbEX 1.0 yields a coalesced 20−90 nm thick Sb_2S_3 absorber composed of grains 1 μm in size by 100−200 nm (Figure 7b, h). The grain size (70−230 nm vs 70−270 nm) and thickness (30−80 nm vs 50−100 nm) of the TU/SbEX 1.5 (Figure 7c,i) and 3.0 absorbers' (Figure 7d,j) values are similar. The TU/SbEX 4.5 absorber is 60−120 nm thick (Figure 7e,k), and 130−380 nm wide, 1 μm long spherulites cover most of the substrate. The flat spherulitic morphology persists at TU/SbEX 6.0 (Figure 7f,l), whereas the film thickness decreases to 30−80 nm.

At TU/SbEX 1.0 and above, the top surface of the coalesced Sb_2S_3 absorber is flattened and deviates from the substrate morphology (Figure 7h−l). The flattening possibly proceeds through curvature-driven self-diffusion,[52] whereby upon heating the amorphous Sb_2S_3 at the tips of the FTO/TiO_2 ridges flows to fill in the pits between them, becoming uneven in local thickness

https://doi.org/10.1021/acsami.3c08547
ACS Appl. Mater. Interfaces 2023, 15, 42622−42636

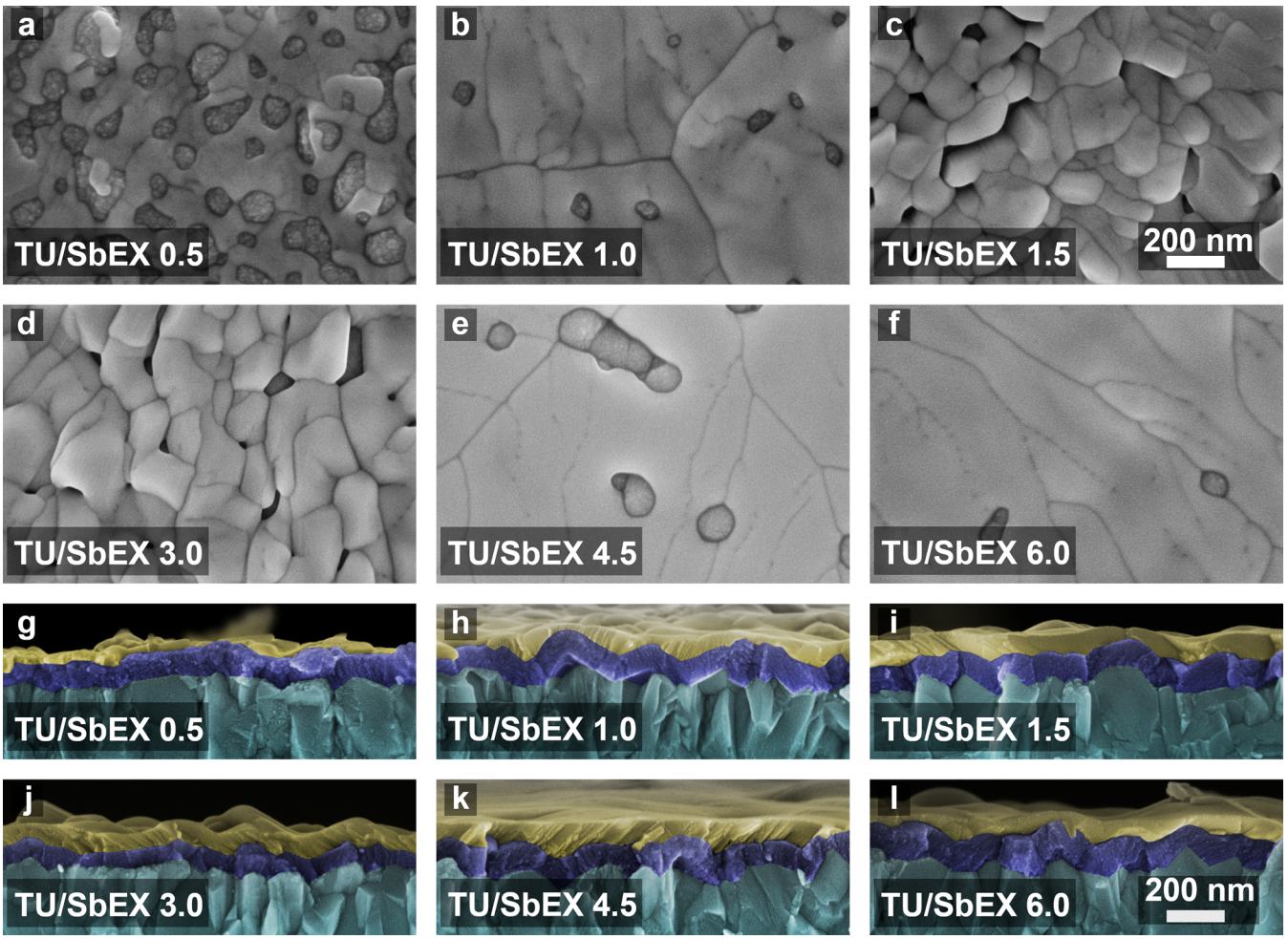

Figure 7. Top-down and cross-sectional SEM images of heat-treated Sb_2S_3 absorbers (in yellow) grown onto a FTO (in cyan)/TiO_2 (in dark blue) substrate at a deposition temperature of 200 °C by USP from a solution with TU/SbEX molar ratios of (a, g) 0.5, (b, h) 1.0, (c, i) 1.5, (d, j) 3.0, (e, k) 4.5, and (f, l) 6.0.

to the extent that the regions of the substrate with the highest aspect ratio are left bare. Consequently, TiO_2/P3HT shunts inevitably form in the vicinity of the uncovered FTO/TiO_2 ridges. Dewetting has to be eliminated to create a denser and pinhole free spray-Sb_2S_3 film either by applying interfacial seed layers[13] or TiO_2 surface modification.[22]

The XRD patterns (Figure 8a) and Raman spectra (Figure 8b) of all of the heat-treated absorbers grown at 200 °C contain only crystalline Sb_2S_3, absent any additional bulk phases. A generalized texture coefficient is required to gauge the proportion of each crystal growth direction in the XRD patterns of Sb_2S_3 vs the powder reference, which is calculated as

$$C_{hkl} = \frac{I_{hkl}/\sum I_{hkl}}{I_{hkl,\mathrm{ref}}/\sum I_{hkl,\mathrm{ref}}} \quad (5)$$

where C_{hkl} is the texture coefficient, I_{hkl} the measured intensity in cps deg, and $I_{hkl,ref}$ the reference intensity of each detected crystallographic growth direction corresponding to the Miller indices (*hkl*) of the No. 62 *Pbnm* system.

The TU/SbEX 0.5−1.0 samples are outliers in terms of the texture coefficient because of the small number and intensity of Sb_2S_3 peaks (Figure 8b), whereas the trend is consistent thereafter. The (110) and (041) texture coefficients dominate in the TU/SbEX 1.5 sample. At TU/SbEX 3.0 the (110) peak disappears. The relative proportion of only the (020), (120), (130), (230), and (041) texture coefficients increases. Next, at TU/SbEX 4.5 the (220) peak disappears. Consequently, the proportion of the (020) and (041) texture coefficients is maximized, diminishing that of the (120), (230), (121), and (221) texture coefficients. At TU/SbEX 6.0, the (121) and (221) peaks disappear, whereas the proportion of the (120) and (141) texture coefficients increases, decreasing the proportion of the (020) and (041) texture coefficients.

Considering the sequential disappearance of the (110), (220), (121), and (221) peaks as the TU/SbEX ratio is increased, the crystal structure of the Sb_2S_3 films can be modified by changing the concentration of TU in the spray solution. Despite the mostly horizontal (*hk*0) growth directions observed in this study, some up to 6.6% efficiency Sb_2S_3 solar cells are based on chemically grown Sb_2S_3 thin films exhibiting larger than usual (020) and (120) peak intensities.[11,12] Thus, we refrain from interpreting preferential growth in the (221), (211), and other (*hk*1) directions as strictly mandatory to achieve high efficiency. Nonetheless, the relative proportion of the (041) and (141) texture coefficients does correlate with the increased average device efficiency presented afterward.

The absorbers grown from the TU/SbEX 0.5 and 1.0 solutions are considerably more transparent at 400 nm wavelength (22 and 6.9%) than films grown using more thiourea

https://doi.org/10.1021/acsami.3c08547
ACS Appl. Mater. Interfaces 2023, 15, 42622−42636

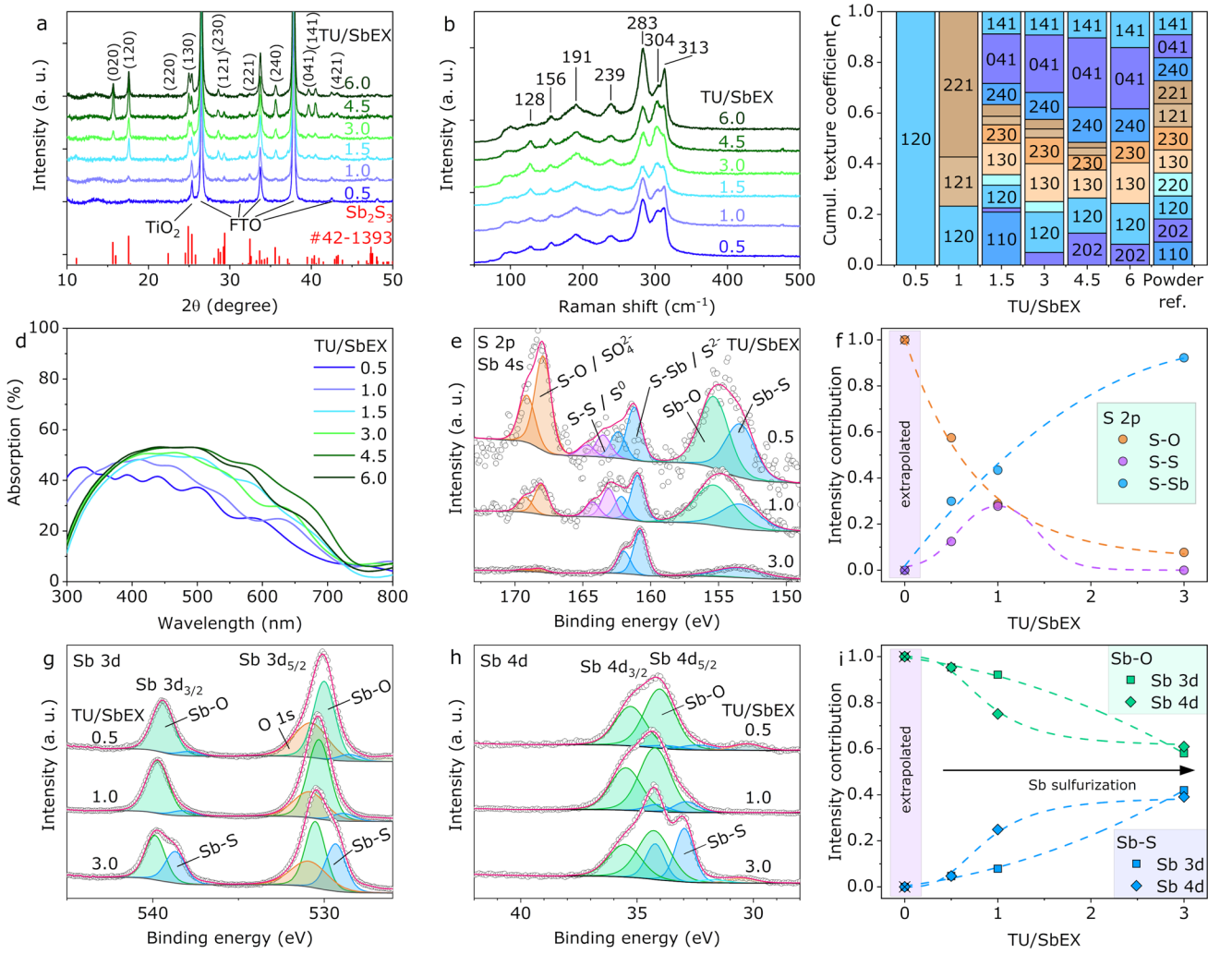

Figure 8. (a) X-ray diffraction (XRD) patterns, (b) Raman spectra, (c) cumulative XRD texture coefficients, (d) absorption spectra, X-ray photoelectron spectroscopy (XPS) results of (e) S 2p region and (f) intensity contributions, extrapolated to TU/SbEX 0, and XPS results of (g) Sb 3d and (h) Sb 4d region, and (i) intensity contributions, extrapolated to TU/SbEX 0, of heat-treated Sb_2S_3 absorbers grown onto glass/FTO/TiO_2 from a solution with variable molar ratios of TU/SbEX.

in the solution (<3%) (Figure S7a). The TU/SbEX 0.5 and 1.0 based absorbers are thus considered to be thin and discontinuous and the remainder conformal.

After heat treatment, the Sb_2S_3 films develop an average reflectance of 33−45% in the 350−750 nm wavelength range (Figure S7b). Such high reflectance could facilitate trapping light between a partially transparent absorber and a back reflector, e.g., Au, Ag, and Ni, in nontransparent cells. A highly reflective absorber is not a concern if it absorbs all incident light, yet is nonetheless detrimental for semitransparent and bifacial solar cells—a primary application for Sb_2S_3 solar cells, because current density is limited by the reduction in absorbed light. Hence, an antireflective absorber or surface texturization at the Sb_2S_3/HTL interface is recommended in semitransparent devices to maximize current density.

The band gap of the heat-treated Sb_2S_3 absorbers is 1.76−1.88 eV from the optical spectra (Figure S7c). As the ratio of TU/SbEX in solution is increased from 0.5 to 1.0, 1.5, 3.0, 4.5, and 6.0, the average absorption in the 350−750 nm wavelength range evolves from 27 to 31, 35, 35, 41, and 38% (Figure 8d), respectively. Observably, more thiourea in the solution yields an absorber with an increased optical thickness until TU/SbEX 4.5. The Sb_2S_3 yield increases probably because the surface is less exposed to air during each deposition cycle, improving adhesion between the amorphous Sb_2S_3 sublayers.

To prove this claim, we recorded XPS spectra of Sb_2S_3 films grown from different TU/SbEX molar ratios. After calibrating for charging offset via auspicious carbon (284.5 eV), S 2p, Sb 4s, Sb 3d, and Sb 4d peak positions (Tables S7−S9) and widths are close to literature values.[6,31]

In the TU/SbEX 0.5 sample, in the S 2p region, doublets attributed to S−S or elementary S, S−Sb (S^{2-}), and S−O (SO_4^{2-}) are observed (Figure 8e). Thus, the explanation provided in the previous section is likely oversimplified for these Sb_2S_3 films due to the various organosulfur compounds observed at ∼168 eV (Figure 8e). Evidently, the concentration of TU is too low to prevent extensive surface oxidation of Sb_2S_3 into Sb_2O_3 and likely formation of polysulfates[7] of the $(Sb_2O_3)_m \cdot (SO_3)_n$ type. Without a protective agent such as TU, Sb_2O_3 is always obtained at a deposition temperature near 200 °C.[25] In the TU/SbEX 1.0 sample, the proportion of the sulfate peaks has diminished, and the proportion of S_0 peaks has increased with respect to the S^{2-} peak intensity (Figure 8f). It is reasonable to conclude that doubling the TU concentration from 0.5 to 1.0

https://doi.org/10.1021/acsami.3c08547
ACS Appl. Mater. Interfaces 2023, 15, 42622−42636

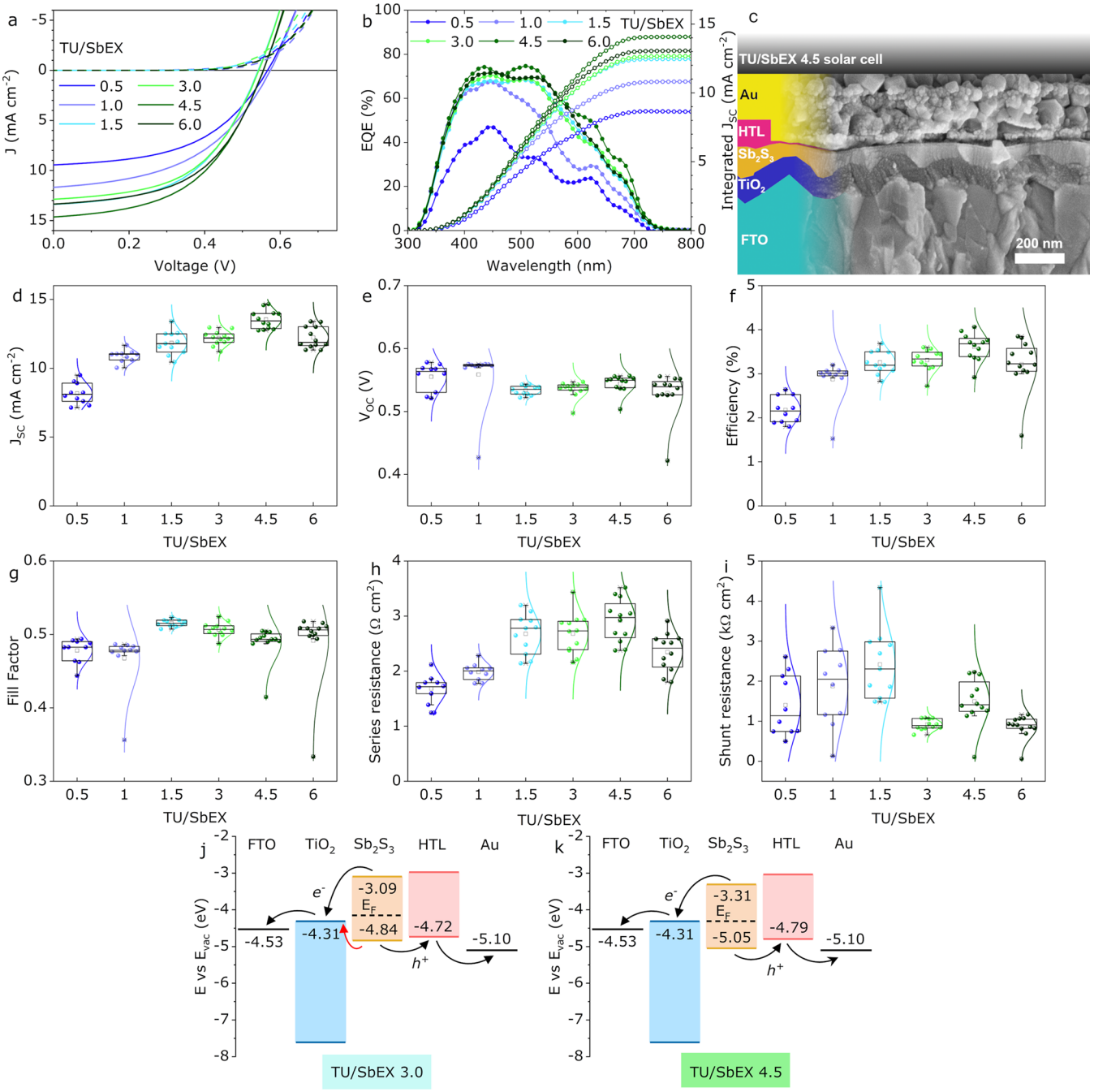

Figure 9. (a) $J-V$ curves and (b) EQE and integrated J_{SC} of best devices based on Sb_2S_3 films grown with a variable molar ratio of TU/SbEX. (c) SEM cross-section of the best device. (Statistics on (d) J_{SC}, (e) V_{OC}, (f) efficiency, (g) fill factor, (h) series resistance, and (i) shunt resistance. Band diagram of the solar cell layer structure at (j) TU/SbEX 3.0 and (k) 4.5.

protects the surface against oxidation, yielding Sb sulfates on the surface, an intermediary elementary sulfur layer, and an unoxidized Sb_2S_3 bulk. Increasing the TU/SbEX molar ratio to 3.0 further suppresses oxidation, as the relative intensity of sulfate and elementary sulfur peaks is drastically decreased.

The Sb 3d region resembles the S 2p range, whereby the Sb−O doublet peaks dominate at TU/SbEX 0.5 and 1.0, and shoulder peaks of Sb−S are present only in the TU/SbEX 3.0 sample (Figure 8g). The difference in the proportion of Sb−S and Sb−O intensities in the Sb 3d region of samples grown in different batches (Figure 2g vs Figure 8g) is primarily attributed to locally varying oxidation (Figure S8). In addition, XPS spectra of the Sb 4d region are presented because there is no overlap with characteristic lines of other elements, as opposed to the unavoidable overlap of the Sb $3d_{5/2}$ and O 1s peaks that leads to uncertainty in data interpretation. The trend of reduced oxidation of Sb_2S_3 as a result of increased TU concentration is also observed in the Sb 4d region (Figure 8h) with the relative proportion of Sb−S being twice as large vs the Sb 3d region (Figure 8i).

The S/Sb atomic ratios from XRF data are 1.07, 1.53, 1.54, and 1.52 for the heat-treated Sb_2S_3 absorbers grown from solutions of TU/SbEX of 0.5, 1.5, 4.5, and 6.0, respectively. The sulfur-poor composition at TU/SbEX 0.5 is caused by partial oxidation during deposition, as proven by XPS, whereas the remaining samples have a nearly stoichiometric composition.

https://doi.org/10.1021/acsami.3c08547
ACS Appl. Mater. Interfaces 2023, 15, 42622−42636

Table 3. Solar Cell Output Characteristics as a Function of the TU/SbEX Molar Ratio in Spray Solution

TU/SbEX	V_{OC}, mV	J_{SC}, mA cm^{-2}		FF, %	η, %	R_S, Ω cm^2	R_{SH}, kΩ cm^2
		$I-V$	EQE				
0.5	567	9.5	8.6	49	2.6	1.2	2.6
	555 ± 22[a]	8.2 ± 0.8		48 ± 2	2.2 ± 0.3	1.7 ± 0.2	1.4 ± 0.8
1.0	574	11.7	10.8	48	3.2	1.8	1.2
	559 ± 46	10.9 ± 0.4		47 ± 4	2.9 ± 0.5	2.0 ± 0.2	1.9 ± 1.0
1.5	543	13.4	12.5	51	3.7	3.2	1.5
	534 ± 7	11.8 ± 0.8		52 ± 1	3.3 ± 0.3	2.7 ± 0.4	2.4 ± 0.9
3.0	544	12.9	12.7	51	3.6	2.9	1.1
	535 ± 13	12.2 ± 0.5		51 ± 1	3.3 ± 0.2	2.7 ± 0.4	0.9 ± 0.1
4.5	556	14.7	14.1	50	4.1	3.0	1.2
	544 ± 15	13.5 ± 0.7		49 ± 2	3.6 ± 0.3	2.9 ± 0.4	1.5 ± 0.6
6.0	556	13.4	13.1	52	3.9	2.6	0.9
	529 ± 36	12.2 ± 0.8		49 ± 5	3.2 ± 0.6	2.3 ± 0.3	0.9 ± 0.3

[a]Average and standard deviation.

Therefore, based on XPS and XRF, it is safe to assume that TU/SbEX in excess of 3.0 is required to grow thoroughly phase pure unoxidized Sb_2S_3 absorbers by USP. In the case of TU/SbEX 0.5, 1.5, 4.5, and 6.0, average Sb_2S_3 film thicknesses are calculated from Sb L_α XRF data as 25, 62, 75, and 53 nm, correlating well with optical absorption, as shown later. TU/SbEX 4.5 yields the maximum Sb_2S_3 film growth rate of 3.8 nm min^{-1}, whereas increasing to TU/SbEX 6.0 slows the film growth rate. We suppose that excess TU blocks some SbEX from reaching the surface of the substrate, repelling SbEX into the aerosol exhaust stream.

The $I-V$ of the best devices (Figure 9a) correlates with absorption, film thickness, and EQE (Figure 9b and Figure S9) because of J_{SC}, as the TU/SbEX 0.5 device is the worst and the 4.5 device is the best. Overall EQE intensity and response in red light are enhanced as TU/SbEX is increased, attributed to increased absorber thickness, culminating in a maximum integral EQE area at TU/SbEX 4.5, whereas the decrease at 6.0 is linked to a thinner absorber. The band gap of the heat-treated Sb_2S_3 absorbers is calculated to be 1.76−1.79 eV from the $(EQE{\cdot}h\nu)^2$ spectra (Figure S10), in agreement with optical measurement results. In addition, J_{SC} of the best cells measured by $I-V$ (Figure 9a) is close to J_{SC} integrated from EQE spectra (Figure 9b and Table 3), exceeding it by 0.2−0.9 mA cm^{-2}. The offset in J_{SC} is attributed to the shape of the light spectrum emitted by the LED and the Xe light source, the vastly different illumination intensity used with these methods, and the photoactivated shunting[26] in Sb_2S_3 devices.

The cross-section of the best TU/SbEX 4.5 Sb_2S_3 solar cell (Figure 9c) illustrates the conformal coverage of TiO_2 on FTO and Sb_2S_3 on TiO_2. However, the top surface of Sb_2S_3 is flat likely because Sb_2S_3 is formed in a liquid−liquid reaction.[15] Furthermore, the surface energy mismatch with TiO_2 causes dewetting of Sb_2S_3,[13,15] and thus poor conformality, which is detrimental to photovoltaic performance because it not only permits electrical and physical shunting between TiO_2 and Au through the ∼20 nm thin P3HT layer but also reduces the uniformity of photocurrent generation.

Considering the average device parameters, increasing TU/SbEX from 0.5 to 4.5 improves the average J_{SC} by a factor of 1.67 (Figure 9d) from 8.1 to 13.5 mA cm^{-2}, whereas V_{OC} (Figure 9e) is relatively unaffected (Table 3). Thus, as TU/SbEX changes from 0.5 to 1.0, 1.5, 3.0, 4.5, and 6.0, efficiency (Figure 9f), driven by J_{SC}, evolves to 2.2, 2.9, 3.3, 3.3, 3.6, and 3.2%, respectively. The fill factor hovers at around 0.5 (Figure 9g) for all devices. The corresponding best devices attain efficiencies of 2.7, 3.2, 3.7, 3.7, 4.1, and 3.9%.

R_S evolves similarly to J_{SC} (Figure 9h). Hence, we ascribe the increase in R_S primarily to an increase in absorber thickness and not TU/SbEX. R_{SH} increases from 1.4 kΩ cm^2 at TU/SbEX 0.5 to 2.4 kΩ cm^2 at 1.5, thereafter decreasing to 0.9 kΩ cm^2 at 6.0 (Figure 9i). R_{SH} is likely enhanced by surface passivation that occurs at the Sb_2S_3/P3HT interface in the TU/SbEX 0.5−1.5 devices owing to the presence of Sb_2O_3, elementary sulfur, sulfates, or a combination of them (Figure 8e). Controlled surface oxidation is a well-known passivation technique to improve Sb_2S_3 solar cell R_{SH} and, thereby, fill factor.[53]

To discern how TU/SbEX affects the solar cell energy levels, the energy level diagrams of the TU/SbEX 3.0 (Figure 9j) and 4.5 (Figure 9k) Sb_2S_3 devices are experimentally determined for every constituent semiconductor layer in the stack. The ionization energy level values are obtained from the PES spectra (Figure S11). The valence band maximum (VBM) of the TU/SbEX 3.0 Sb_2S_3 absorber is positioned at −4.84 eV vs vacuum energy, resulting in a 0.53 eV potential difference with the conduction band minimum (CBM) of TiO_2. As a result, a favorable recombination pathway is created for photogenerated holes at the TiO_2/Sb_2S_3 interface. At the same time, there is a 0.38 eV offset in the VBM of P3HT and Au, creating an undesired back contact barrier. Furthermore, the offset between the CBM of TiO_2 and the CBM of Sb_2S_3 is 1.22 eV, which is considered suboptimal for electron extraction. Increasing TU/SbEX to 4.5 causes multiple changes. The VBM and CBM of the Sb_2S_3 absorber respectively downshift to −5.05 and −3.31 eV (Figure 9k), respectively. Therefore, the TiO_2 CBM and Sb_2S_3 CBM offsets are reduced to 1.00 eV, enhancing electron extraction efficiency. The TiO_2 CBM and Sb_2S_3 VBM offset increases to 0.74 eV, resulting in a net 0.21 eV improvement in blocking hole recombination at the TiO_2/Sb_2S_3 interface. Moreover, the VBM of P3HT is downshifted to −4.79 eV,

https://doi.org/10.1021/acsami.3c08547
ACS Appl. Mater. Interfaces 2023, 15, 42622−42636

possibly due to the downshift of the CBM and VBM of the underlying Sb_2S_3 layer. Thereby, the P3HT/Au back contact barrier is reduced to 0.21 eV, which is unlikely to form a severe back contact barrier. The downshift in the VBM of Sb_2S_3 at TU/SbEX 4.5 vs 3.0 is ascribed to increased Sb_2S_3 phase purity at the Sb_2S_3/P3HT interface because of suppressed oxidation during deposition.

CONCLUSIONS

Increasing the deposition temperature of Sb_2S_3 above 200 °C yielded a thicker and bulk-phase-pure yet discontinuous absorber due to dewetting during the liquid-phase decomposition of SbEX to Sb_2S_3. The deteriorated morphology of the absorber promoted shunting and decreased short-circuit current density in solar cells. According to temperature-dependent current−voltage analysis, the solar cell based on the Sb_2S_3 absorber grown at 200 °C was mainly limited by interface and tunneling related recombination, whereas the 260 °C device was affected by bulk recombination, as well. Further analysis by DLTS revealed that increasing the deposition temperature affected the concentration of V_{Sb}, resulting in increased open-circuit voltage in the device based on Sb_2S_3 grown at 260 °C. Increasing the molar ratio of thiourea to SbEX increased the Sb_2S_3 film growth rate by suppressing bulk and surface oxidation and decreasing the number and proportion of crystal growth directions lying horizontally on the substrate. Thereby, the formation of a continuous and flat absorber film was promoted, yielding proportionally higher short-circuit current density as the thickness, bulk, and surface purity of the absorber increased. Overall, the best solar cell efficiency of 4.1% was achieved at a TU/SbEX molar ratio of 4.5 at an average absorber thickness of 75 nm. Increasing the molar ratio from 3.0 to 4.5 resulted in an ∼0.2 eV more favorable energy level alignment at both the Sb_2S_3/P3HT and the P3HT/Au interface. Our findings highlight the importance of developing synthesis conditions to achieve the best solar cell device performance for an Sb_2S_3 absorber layer pertaining to the chosen deposition method, experimental setup, and precursors.

ASSOCIATED CONTENT

Supporting Information

The Supporting Information is available free of charge at https://pubs.acs.org/doi/10.1021/acsami.3c08547.

List of chemicals used, additional UV−vis and EQE spectra, UV−vis spectra, *I*−*V* statistics, and optical microscope images of the deposition time series, SEM images, tabulated *I*−*V*−*T* and XPS fit results, Pearson correlation graphs, 2D XPS data, and PES fit curves for the partial solar cell stacks (PDF)

AUTHOR INFORMATION

Corresponding Authors

Jako S. Eensalu − *Laboratory of Thin Film Chemical Technologies, Department of Materials and Environmental Technology, Tallinn University of Technology, Tallinn 19086, Estonia; Max IV Laboratory, Lund University, Lund 224 84, Sweden;* orcid.org/0000-0002-4312-0227; Email: jako.eensalu@taltech.ee

Malle Krunks − *Laboratory of Thin Film Chemical Technologies, Department of Materials and Environmental Technology, Tallinn University of Technology, Tallinn 19086, Estonia*; Email: malle.krunks@taltech.ee

Authors

Sreekanth Mandati − *Laboratory of Thin Film Chemical Technologies, Department of Materials and Environmental Technology, Tallinn University of Technology, Tallinn 19086, Estonia;* orcid.org/0000-0002-3317-271X

Christopher H. Don − *Department of Physics/Stephenson Institute for Renewable Energy, University of Liverpool, Liverpool L69 3BX, United Kingdom*

Harry Finch − *Department of Physics/Stephenson Institute for Renewable Energy, University of Liverpool, Liverpool L69 3BX, United Kingdom*

Vinod R. Dhanak − *Department of Physics/Stephenson Institute for Renewable Energy, University of Liverpool, Liverpool L69 3BX, United Kingdom*

Jonathan D. Major − *Department of Physics/Stephenson Institute for Renewable Energy, University of Liverpool, Liverpool L69 3BX, United Kingdom*

Raitis Grzibovskis − *Institute of Solid State Physics, University of Latvia, Riga LV-1063, Latvia*

Aile Tamm − *Laboratory of Thin Film Technology, Institute of Physics, Tartu University, 50411 Tartu, Estonia;* orcid.org/0000-0002-0547-0824

Peeter Ritslaid − *Laboratory of Thin Film Technology, Institute of Physics, Tartu University, 50411 Tartu, Estonia;* orcid.org/0000-0002-3603-2237

Raavo Josepson − *Division of Physics, Department of Cybernetics, Tallinn University of Technology, Tallinn 19086, Estonia*

Tanel Käämbre − *Max IV Laboratory, Lund University, Lund 224 84, Sweden; Laboratory of X-Ray Spectroscopy, Institute of Physics, Tartu University, 50411 Tartu, Estonia*

Aivars Vembris − *Institute of Solid State Physics, University of Latvia, Riga LV-1063, Latvia*

Nicolae Spalatu − *Laboratory of Thin Film Chemical Technologies, Department of Materials and Environmental Technology, Tallinn University of Technology, Tallinn 19086, Estonia;* orcid.org/0000-0003-0234-2170

Ilona Oja Acik − *Laboratory of Thin Film Chemical Technologies, Department of Materials and Environmental Technology, Tallinn University of Technology, Tallinn 19086, Estonia*

Complete contact information is available at: https://pubs.acs.org/10.1021/acsami.3c08547

Author Contributions

The manuscript was written through contributions of all authors. All authors have given approval to the final version of the manuscript.

Notes

The authors declare no competing financial interest.

ACKNOWLEDGMENTS

J.S.E. thanks Beamline Specialist Dr. Weimin Wang for instructing how to operate the solid-state endstation at the FinEstBeAMS beamline at Max IV Lab. The authors also thank the two anonymous reviewers for their contribution. This reearch was funded by the Estonian Research Council project PRG627, the Estonian State Shared Service Center project AR20015, the Estonian Research Council project TT20 "(MAX-TEENUS)", the Archimedes Foundation project AR17092 "(NAMUR+)", the Center of Excellence project TAR16016EK, and the European Commission project VFP20035 5GSOLAR-

952509. Funding for the work was provided by the EPSRC via EP/N014057/1 and EP/W03445X/1. The present work was financially supported by the Estonian Research Council (PRG4), and this research was also supported by the EU through the European Regional Development Fund Center of Excellence project TK134- "Emerging orders in quantum and nanomaterials". The Institute of Solid State Physics, University of Latvia as the Centre of Excellence has received funding from the European Union's Horizon 2020 Framework Programme H2020-WIDESPREAD-01-2016- 2017-TeamingPhase2 under grant agreement No. 739508, project CAMART^2. Financial support was also provided by the European Regional Development Fund (grant No. MAX-TEENUS 2014-2020.4.01.20-0278 to University of Tartu). We acknowledge MAX IV Laboratory for offline and beam time on the SSES branch of Beamline FinEstBeAMS as part of in-house research. Research conducted at MAX IV, a Swedish national user facility, is supported by the Swedish Research council under contract 2018-07152, the Swedish Governmental Agency for Innovation Systems under contract 2018-04969, and Formas under contract 2019-02496.

■ ABBREVIATIONS

α, absorption coefficient; CBM, conduction band minimum; DFT, density functional theory; DLTS, deep level transient spectroscopy; EQE, external quantum efficiency; FF, fill factor; FTO, fluorine-doped tin oxide; η, power conversion efficiency; HTL, hole transport layer; J_{SC}, short-circuit current density; PES, photoelectron emission spectroscopy; PV, photovoltaic; P3HT, poly(3-hexylthiophene-2,5-diyl); R_S, series resistance; R_{SH}, shunt resistance; Sb_S, sulfur antimony antisite; SEM, scanning electron microscope; TU/SbEX, thiourea to antimony ethyl xanthate molar ratio; VBM, valence band maximum; V_{OC}, open-circuit voltage; V_{Sb}, antimony vacancy; V_S, sulfur vacancy; XPS, X-ray photoelectron spectroscopy; XRD, X-ray diffraction; XRF, X-ray fluorescence

■ REFERENCES

(1) *Solar Energy*; Richter, C., Lincot, D., Gueymard, C. A., Eds.; Springer: 2012; pp 170−173.
(2) Greenwood, N. N.; Earnshaw, A. Arsenic, Antimony and Bismuth. In *Chemistry of the Elements*, 2nd ed.; Butterworth-Heinemann: 1997; pp 581−582.
(3) U.S. Geological Survey. *Mineral Commodity Summaries 2022*; U.S. Geological Survey: 2022; p 202. DOI: 10.3133/mcs2022.
(4) Dong, J.; Liu, Y.; Wang, Z.; Zhang, Y. Boosting V_{OC} of Antimony Chalcogenide Solar Cells: A Review on Interfaces and Defects. *Nano Select* **2021**, *2* (10), 1818−1848.
(5) Gutiérrez, Y.; Ovvyan, A. P.; Santos, G.; Juan, D.; Rosales, S. A.; Junquera, J.; García-Fernández, P.; Dicorato, S.; Giangregorio, M. M.; Dilonardo, E.; Palumbo, F.; Modreanu, M.; Resl, J.; Ishchenko, O.; Garry, G.; Jonuzi, T.; Georghe, M.; Cobianu, C.; Hingerl, K.; Cobet, C.; Moreno, F.; Pernice, W. H. P.; Losurdo, M. Interlaboratory Study on Sb_2S_3 Interplay between Structure, Dielectric Function, and Amorphous-to-Crystalline Phase Change for Photonics. *iScience* **2022**, *25* (6), 104377.
(6) Büttner, P.; Scheler, F.; Döhler, D.; Barr, M. K. S.; Bosch, M.; Rey, M.; Yokosawa, T.; Hinz, S.; Maultzsch, J.; Spiecker, E.; Vogel, N.; Mínguez-Bacho, I.; Bachmann, J. Continuous, Crystalline Sb_2S_3 Ultrathin Light Absorber Coatings in Solar Cells Based on Photonic Concentric p-i-n Heterojunctions. *Nano Energy* **2022**, *103*, No. 107820.
(7) Thorneycroft, W. E. Antimony and Sulphur. In *Antimony and Bismuth*; Friend, J. N., Ed.; ; Charles Griffin: 1936; A Text Book of Inorganic Chemistry, Vol. *VI*, Part V, pp 97−101.
(8) Kim, D.-H.; Lee, S.-J.; Park, M. S.; Kang, J.-K.; Heo, J. H.; Im, S. H.; Sung, S.-J. Highly Reproducible Planar Sb_2S_3-Sensitized Solar Cells Based on Atomic Layer Deposition. *Nanoscale* **2014**, *6* (23), 14549−14554.
(9) Wang, S.; Zhao, Y.; Che, B.; Li, C.; Chen, X.; Tang, R.; Gong, J.; Wang, X.; Chen, G.; Chen, T.; Li, J.; Xiao, X. A Novel Multi-Sulfur Source Collaborative Chemical Bath Deposition Technology Enables 8%-Efficiency Sb_2S_3 Planar Solar Cells. *Adv. Mater.* **2022**, *34* (41), No. 2206242.
(10) Yang, Z.; Wang, X.; Chen, Y.; Zheng, Z.; Chen, Z.; Xu, W.; Liu, W.; Yang, Y.; Zhao, J.; Chen, T.; Zhu, H. Ultrafast Self-Trapping of Photoexcited Carriers Sets the Upper Limit on Antimony Trisulfide Photovoltaic Devices. *Nat. Commun.* **2019**, *10* (1), 4540.
(11) Tang, R.; Wang, X.; Jiang, C.; Li, S.; Liu, W.; Ju, H.; Yang, S.; Zhu, C.; Chen, T. N-Type Doping of Sb_2S_3 Light-Harvesting Films Enabling High-Efficiency Planar Heterojunction Solar Cells. *ACS Appl. Mater. Interfaces* **2018**, *10* (36), 30314−30321.
(12) Jiang, C.; Tang, R.; Wang, X.; Ju, H.; Chen, G.; Chen, T. Alkali Metals Doping for High-Performance Planar Heterojunction Sb_2S_3 Solar Cells. *Solar RRL* **2019**, *3* (1), No. 1800272.
(13) Büttner, P.; Scheler, F.; Pointer, C.; Döhler, D.; Barr, M. K. S.; Koroleva, A.; Pankin, D.; Hatada, R.; Flege, S.; Manshina, A.; Young, E. R.; Mínguez-Bacho, I.; Bachmann, J. Adjusting Interfacial Chemistry and Electronic Properties of Photovoltaics Based on a Highly Pure Sb_2S_3 Absorber by Atomic Layer Deposition. *ACS Appl. Energy Mater.* **2019**, *2* (12), 8747−8756.
(14) Guo, L.; Zhang, B.; Li, S.; Zhang, Q.; Buettner, M.; Li, L.; Qian, X.; Yan, F. Scalable and Efficient Sb_2S_3 Thin-Film Solar Cells Fabricated by Close Space Sublimation. *APL Materials* **2019**, *7* (4), No. 041105.
(15) Eensalu, J. S.; Katerski, A.; Kärber, E.; Oja Acik, I.; Mere, A.; Krunks, M. Uniform Sb_2S_3 Optical Coatings by Chemical Spray Method. *Beilstein J. Nanotechnol.* **2019**, *10*, 198−210.
(16) Choi, Y. C.; Lee, D. U.; Noh, J. H.; Kim, E. K.; Seok, S. I. Highly Improved Sb_2S_3 Sensitized-Inorganic−Organic Heterojunction Solar Cells and Quantification of Traps by Deep-Level Transient Spectroscopy. *Adv. Funct. Mater.* **2014**, *24* (23), 3587−3592.
(17) European Commission. Communication from the Commission to the European Parliament, The Council, The European Economic and Social Committee and the Committee of the regions Critical Raw Materials Resilience: Charting a Path towards Greater Security and Sustainability, 2020. https://eur-lex.europa.eu/legal-content/EN/TXT/?uri=CELEX:52020DC0474.
(18) Department of the Interior; Office of the Secretary. Final List of Critical Minerals 2018, 2018. https://www.federalregister.gov/documents/2018/05/18/2018-10667/final-list-of-critical-minerals-2018.
(19) 2022 Critical Minerals Strategy, 2022. https://www.industry.gov.au/publications/critical-minerals-strategy-2022.
(20) Lee, S.-J.; Sung, S.-J.; Yang, K.-J.; Kang, J.-K.; Kim, J. Y.; Do, Y. S.; Kim, D.-H. Approach to Transparent Photovoltaics Based on Wide Band Gap Sb_2S_3 Absorber Layers and Optics-Based Device Optimization. *ACS Appl. Energy Mater.* **2020**, *3* (12), 12644−12651.
(21) Kumar, P.; You, S.; Vomiero, A. CuSCN as a Hole Transport Layer in an Inorganic Solution-Processed Planar Sb_2S_3 Solar Cell, Enabling Carbon-Based and Semitransparent Photovoltaics. *J. Mater. Chem. C* **2022**, *10* (43), 16273−16282.
(22) Han, J.; Pu, X.; Zhou, H.; Cao, Q.; Wang, S.; He, Z.; Gao, B.; Li, T.; Zhao, J.; Li, X. Synergistic Effect through the Introduction of Inorganic Zinc Halides at the Interface of TiO_2 and Sb_2S_3 for High-Performance Sb_2S_3 Planar Thin-Film Solar Cells. *ACS Appl. Mater. Interfaces* **2020**, *12* (39), 44297−44306.
(23) Han, J.; Wang, S.; Yang, J.; Guo, S.; Cao, Q.; Tang, H.; Pu, X.; Gao, B.; Li, X. Solution-Processed Sb_2S_3 Planar Thin Film Solar Cells with a Conversion Efficiency of 6.9% at an Open Circuit Voltage of 0.7 V Achieved via Surface Passivation by a $SbCl_3$ Interface Layer. *ACS Appl. Mater. Interfaces* **2020**, *12* (4), 4970−4979.
(24) Li, J.; Liu, X.; Yao, J. The Enhanced Photovoltaic Performance of Sb_2S_3 Solar Cells by Thermal Decomposition of Antimony Ethyl Xanthate with Thiourea Doping. *Energy Technology* **2020**, *8* (4), 1900841.

(25) Eensalu, J. S.; Tõnsuaadu, K.; Oja Acik, I.; Krunks, M. Sb_2S_3 Thin Films by Ultrasonic Spray Pyrolysis of Antimony Ethyl Xanthate. *Mater. Sci. Semicond. Process.* **2022**, *137*, No. 106209.
(26) Eensalu, J. S.; Katerski, A.; Kärber, E.; Weinhardt, L.; Blum, M.; Heske, C.; Yang, W.; Oja Acik, I.; Krunks, M. Semitransparent Sb_2S_3 Thin Film Solar Cells by Ultrasonic Spray Pyrolysis for Use in Solar Windows. *Beilstein J. Nanotechn.* **2019**, *10*, 2396−2409.
(27) Tamm, A.; Acik, I. O.; Arroval, T.; Kasikov, A.; Seemen, H.; Marandi, M.; Krunks, M.; Mere, A.; Kukli, K.; Aarik, J. Plasmon Resonance Effect Caused by Gold Nanoparticles Formed on Titanium Oxide Films. *Thin Solid Films* **2016**, *616*, 449−455.
(28) Hobson, T. D. C.; Durose, K. Protocols for the Miller Indexing of Sb_2Se_3 and a Non-x-Ray Method of Orienting Its Single Crystals. *Mater. Sci. Semicond. Process.* **2021**, *127*, No. 105691.
(29) Whittles, T. J.; Burton, L. A.; Skelton, J. M.; Walsh, A.; Veal, T. D.; Dhanak, V. R. Band Alignments, Valence Bands, and Core Levels in the Tin Sulfides SnS, SnS_2, and Sn_2S_3: Experiment and Theory. *Chem. Mater.* **2016**, *28* (11), 3718−3726.
(30) Chernenko, K.; Kivimaki, A.; Parna, R.; Wang, W.; Sankari, R.; Leandersson, M.; Tarawneh, H.; Pankratov, V.; Kook, M.; Kukk, E.; Reisberg, L.; Urpelainen, S.; Kaambre, T.; Siewert, F.; Gwalt, G.; Sokolov, A.; Lemke, S.; Alimov, S.; Knedel, J.; Kutz, O.; Seliger, T.; Valden, M.; Hirsimaki, M.; Kirm, M.; Huttula, M. Performance and Characterization of the FinEstBeAMS Beamline at the MAX IV Laboratory. *J. Synchrotron Radiat.* **2021**, *28*, 1620−1630.
(31) Zakaznova-Herzog, V. P.; Harmer, S. L.; Nesbitt, H. W.; Bancroft, G. M.; Flemming, R.; Pratt, A. R. High Resolution XPS Study of the Large-Band-Gap Semiconductor Stibnite (Sb_2S_3): Structural Contributions and Surface Reconstruction. *Surf. Sci.* **2006**, *600* (2), 348−356.
(32) Hobson, T. D. C.; Phillips, L. J.; Hutter, O. S.; Durose, K.; Major, J. D. Defect Properties of Sb_2Se_3 Thin Film Solar Cells and Bulk Crystals. *Appl. Phys. Lett.* **2020**, *116* (26), 261101.
(33) Eensalu, J. S.; Tõnsuaadu, K.; Adamson, J.; Oja Acik, I.; Krunks, M. Thermal Decomposition of Tris(O-Ethyldithiocarbonato)-Antimony(III)—a Single-Source Precursor for Antimony Sulfide Thin Films. *J. Therm. Anal. Calorim.* **2022**, *147* (8), 4899−4913.
(34) Kärber, E.; Katerski, A.; Oja Acik, I.; Mere, A.; Mikli, V.; Krunks, M. Sb_2S_3 Grown by Ultrasonic Spray Pyrolysis and Its Application in a Hybrid Solar Cell. *Beilstein J. Nanotechnol.* **2016**, *7*, 1662−1673.
(35) Don, C. H.; Shiel, H.; Hobson, T. D. C.; Savory, C. N.; Swallow, J. E. N.; Smiles, M. J.; Jones, L. A. H.; Featherstone, T. J.; Thakur, P. K.; Lee, T.-L.; Durose, K.; Major, J. D.; Dhanak, V. R.; Scanlon, D. O.; Veal, T. D. Sb $5s^2$ Lone Pairs and Band Alignment of Sb_2Se_3: A Photoemission and Density Functional Theory Study. *J. Mater. Chem. C* **2020**, *8* (36), 12615−12622.
(36) Zhao, Y.; Wang, S.; Li, C.; Che, B.; Chen, X.; Chen, H.; Tang, R.; Wang, X.; Chen, G.; Wang, T.; Gong, J.; Chen, T.; Xiao, X.; Li, J. Regulating Deposition Kinetics via a Novel Additive-Assisted Chemical Bath Deposition Technology Enables Fabrication of 10.57%-Efficiency Sb_2Se_3 Solar Cells. *Energy Environ. Sci.* **2022**, *15*, 5118.
(37) Shiel, H.; Hobson, T. D. C.; Hutter, O. S.; Phillips, L. J.; Smiles, M. J.; Jones, L. A. H.; Featherstone, T. J.; Swallow, J. E. N.; Thakur, P. K.; Lee, T.-L.; Major, J. D.; Durose, K.; Veal, T. D. Band Alignment of Sb_2O_3 and Sb_2Se_3. *J. Appl. Phys. (Melville, NY, U. S.)* **2021**, *129* (23), 235301.
(38) Fleck, N.; Hutter, O. S.; Phillips, L. J.; Shiel, H.; Hobson, T. D. C.; Dhanak, V. R.; Veal, T. D.; Jäckel, F.; Durose, K.; Major, J. D. How Oxygen Exposure Improves the Back Contact and Performance of Antimony Selenide Solar Cells. *ACS Appl. Mater. Interfaces* **2020**, *12* (47), 52595−52602.
(39) Castner, D. G.; Hinds, K.; Grainger, D. W. X-Ray Photoelectron Spectroscopy Sulfur 2p Study of Organic Thiol and Disulfide Binding Interactions with Gold Surfaces. *Langmuir* **1996**, *12* (21), 5083−5086.
(40) Hobson, T. D. C.; Shiel, H.; Savory, C. N.; Swallow, J. E. N.; Jones, L. A. H.; Featherstone, T. J.; Smiles, M. J.; Thakur, P. K.; Lee, T.-L.; Das, B.; Leighton, C.; Zoppi, G.; Dhanak, V. R.; Scanlon, D. O.; Veal, T. D.; Durose, K.; Major, J. D. P-Type Conductivity in Sn-Doped Sb_2Se_3. *J. Phys.: Energy* **2022**, *4* (4), No. 045006.
(41) Yin, Y.; Wu, C.; Tang, R.; Jiang, C.; Jiang, G.; Liu, W.; Chen, T.; Zhu, C. Composition Engineering of Sb_2S_3 Film Enabling High Performance Solar Cells. *Sci. Bull.* **2019**, *64* (2), 136−141.
(42) Darga, A.; Mencaraglia, D.; Longeaud, C.; Savenije, T. J.; O'Regan, B.; Bourdais, S.; Muto, T.; Delatouche, B.; Dennler, G. On Charge Carrier Recombination in Sb_2S_3 and Its Implication for the Performance of Solar Cells. *J. Phys. Chem. C* **2013**, *117* (40), 20525−20530.
(43) Rau, U.; Schock, H. W. Electronic Properties of Cu(In,Ga)Se_2 Heterojunction Solar Cells−Recent Achievements, Current Understanding, and Future Challenges. *Appl. Phys. A: Mater. Sci. Process.* **1999**, *69* (2), 131−147.
(44) Wang, R.; Wang, Y.; Pan, Y.; Qin, D.; Weng, G.; Hu, X.; Tao, J.; Luo, X.; Chen, S.; Zhu, Z.; Chu, J.; Akiyama, H. Improving the Performance of Sb_2S_3 Thin-Film Solar Cells by Optimization of VTD Source-Substrate Proximity. *Sol. Energy* **2021**, *220*, 942−948.
(45) Hu, X.; Tao, J.; Wang, R.; Wang, Y.; Pan, Y.; Weng, G.; Luo, X.; Chen, S.; Zhu, Z.; Chu, J.; Akiyama, H. Fabricating over 7%-Efficient $Sb_2(S,Se)_3$ Thin-Film Solar Cells by Vapor Transport Deposition Using Sb_2Se_3 and Sb_2S_3 Mixed Powders as the Evaporation Source. *J. Power Sources* **2021**, *493*, No. 229737.
(46) Kauk-Kuusik, M.; Timmo, K.; Muska, K.; Pilvet, M.; Krustok, J.; Danilson, M.; Mikli, V.; Josepson, R.; Grossberg-Kuusk, M. Reduced Recombination through CZTS/CdS Interface Engineering in Monograin Layer Solar Cells. *J. Phys.: Energy* **2022**, *4* (2), No. 024007.
(47) Lee, S. W.; Keum, H.-S.; Kim, H. S.; Kim, H. J.; Ahn, K.; Lee, D. R.; Kim, J. H.; Lee, H. H. Temperature-Dependent Evolution of Poly(3-Hexylthiophene) Type-II Phase in a Blended Thin Film. *Macromol. Rapid Commun.* **2016**, *37* (3), 203−208.
(48) Grigas, J.; Karpus, A. Dielectric Properties of Sb_2S_3 Crystals. *Phys. Solid State* **1967**, *9*, 2882−2886.
(49) Nadenau, V.; Rau, U.; Jasenek, A.; Schock, H. W. Electronic Properties of $CuGaSe_2$-Based Heterojunction Solar Cells. Part I. Transport Analysis. *J. Appl. Phys. (Melville, NY, U. S.)* **2000**, *87* (1), 584−593.
(50) Beck, H. E.; Zimmermann, N. E.; McVicar, T. R.; Vergopolan, N.; Berg, A.; Wood, E. F. Present and Future Köppen-Geiger Climate Classification Maps at 1-Km Resolution. *Sci. Data* **2018**, *5* (1), No. 180214.
(51) Artegiani, E.; Major, J. D.; Shiel, H.; Dhanak, V.; Ferrari, C.; Romeo, A. How the Amount of Copper Influences the Formation and Stability of Defects in CdTe Solar Cells. *Sol. Energy Mater. Sol. Cells* **2020**, *204*, No. 110228.
(52) Thompson, C. V. Solid-State Dewetting of Thin Films. *Annu. Rev. Mater. Res.* **2012**, *42* (1), 399−434.
(53) Itzhaik, Y.; Niitsoo, O.; Page, M.; Hodes, G. Sb_2S_3-Sensitized Nanoporous TiO_2 Solar Cells. *J. Phys. Chem. C* **2009**, *113* (11), 4254−4256.

https://doi.org/10.1021/acsami.3c08547
ACS Appl. Mater. Interfaces 2023, 15, 42622−42636